TECHNOLOGY • RESEARCH HIGHLIGHTS • VISIONS • SCIENCE •
127

The effect of stress state on groundwater flow in bedrock

Simulations of in situ experiments

Karita Kajanto

VTT

VTT TECHNOLOGY 127

The effect of stress state on groundwater flow in bedrock

Simulations of in situ experiments

Karita Kajanto

The effect of stress state on groundwater flow in bedrock
Simulations of in situ experiments

Jännitystilan vaikutus pohjaveden virtaukseen kallioperässä. Paikkatutkimustulosten mallinnusta. **Karita Kajanto.** Espoo 2013. VTT Technology 127. 59 p.

Abstract

The effect of the stress state on the permeability of bedrock for groundwater was studied by simulating an in situ experiment. Previous studies show that the dependency of permeability on stress can have a significant effect on flow. Several models have been developed, but little has been done in order to develop models suitable for in situ applications, such as the deep underground repositories for spent nuclear fuel. In repositories, stress state evolves during the long time period considered in safety assessment. The effect of the changing flow pattern, due to the evolving stress, has to be estimated for, e.g., radionuclide transport calculations.

Previous work done in the field was reviewed, existing relations between stress and permeability were analysed, and suitable relations were selected for the modelling cases. Rock mass permeability and discrete fracture permeability were treated separately. One new empirical model for fracture permeability was presented and three models were further developed to be more suitable for 3-D implementation. Simulations followed in situ experiments conducted in Äspö Hard Rock Laboratory. The modelling geometry was constructed based on the experimental setup and the fracture information from the location. The overall stress state in the area was known and the effect of the measurement tunnel and boreholes was computed. The stress state was used to compute the groundwater flow, and the applicability of the chosen models for in situ modelling was analysed. COMSOL Multiphysics was used as the tool for the simulations.

The simulation results followed the measurements reasonably well, but differences were found with one model. The results show that differences between most of the models were relatively small if inflow rates were compared, however, differences between flow patterns were found. Stress dependency could partly explain observed phenomena and qualitative behaviour. Moreover, some of the fracture models were able to identify fractures prone to deformation.

Keywords permeability, stress, in situ, bedrock, groundwater

Jännitystilan vaikutus pohjaveden virtaukseen kallioperässä
Paikkatutkimustulosten mallinnusta

The effect of stress state on groundwater flow in bedrock. Simulations of in situ experiments.
Karita Kajanto. Espoo 2013. VTT Technology 127. 59 s.

Tiivistelmä

Jännitystilan vaikutusta kallioperän permeabiliteettiin vedelle tutkittiin simuloimalla in situ -tilannetta. Aiemmat tutkimukset ovat osoittaneet, että permeabiliteetin riippuvuus jännitystilasta voi vaikuttaa merkittävästi kallion pohjavesivirtaukseen. Erilaisia malleja aiheesta on kehitetty, mutta in situ -mallinnukseen soveltuvien mallien kehitys on jäänyt vähemmälle. Turvallisuusanalyysin pitkän ajanjakson aikana jännitystila kalliossa loppusijoitussyvyydellä muuttuu. Muuttuvan jännityksen virtaukseen aiheuttamat muutokset tulee ottaa huomioon radionuklidien kulkeutumislaskennassa.

Tässä työssä käytiin läpi alan aiempia tutkimuksia, analysoitiin kehitettyjä jännityksen ja permeabiliteetin välisiä malleja sekä valittiin erilaisia tutkittavalle kivityypille soveltuvia malleja mallinnustapauksissa käytettäviksi. Kiviaineksen permeabiliteettia ja yksittäisten rakojen permeabiliteettia käsiteltiin erikseen. Uusi empiirinen rakopermeabiliteettimalli esiteltiin ja aiempia malleja kehitettiin paremmin in situ -mallinnukseen sopiviksi. Simulaatiotapaukset laadittiin Äspö Hard Rock Laboratoryssa tehtyjen mittausten mukaisesti. Laskentageometria vastasi koejärjestelyjä ja alueelta tehtyjä havaintoja. Alueen keskimääräinen jännitystila tunnetaan, ja sen avulla laskettiin mittaustunnelin ja reikien vaikutus mallinnusalueella. Valittujen mallien soveltuvuutta in situ -mallinnukseen analysoitiin. Laskenta suoritettiin COMSOL Multiphysics -ohjelmistolla.

Mallien tulokset noudattivat mittauksia in situ -mallinnustuloksiksi hyvin, mutta joissain tapauksissa esiintyi selviä eroja. Virtaamatuloksien väliset erot useiden mallien kesken olivat suhteellisen pieniä. Virtausjakaumista löytyi selkeitä eroja, ja jännitystilariippuvuudella voinee selittää joitain tuloksia ja käyttäytymistä. Lisäksi havaittiin, että eräillä rakomalleilla pystyy tunnistamaan raot, joilla on muita suurempi todennäköisyys deformaatioon.

Avainsanat permeability, stress, in situ, bedrock, groundwater

Preface

This Thesis was written in the Nuclear Waste Management team of VTT during 2013. Many people have contributed in the course of the process. I would like to thank my instructor Veli-Matti Pulkkanen for his guidance and ideas during the project, for the conversations, and for teaching me an excellent introductory lecture on structural mechanics. This Thesis was supervised by professor Rainer Salomaa, who I would like to thank for his instructions on studies, and for commenting the manuscript, as well as my previous special assignments. My team leader Kari Rasilainen and professor Markus Olin have both commented the manuscript and given helpful ideas. I would like to thank Åsa Fransson from Chalmers University and Marcus Wahlqvist from Cascade Computing AB for kindly answering my questions concerning the measurements and data.

I would also like to thank my family and friends for their patience and encouragement. My dance group and teachers have provided a vital distraction from the daily work, fresh ideas, and a different perspective on life. I thank Niko for his unwavering love, support, and encouragement, and for all those walks around Otaniemi.

Otaniemi, 24$^{\text{th}}$ September, 2013

Karita Kajanto

Contents

Symbols and Abbreviations

Symbols

$\boldsymbol{\varepsilon}$	Strain (tensor)
$\varepsilon_{\mathrm{VOL}}$	Volumetric strain
θ	Dip
$\boldsymbol{\kappa}$	Rock permeability (tensor)
κ	Rock permeability (scalar)
κ_0	Rock permeability in the unstressed state
$\boldsymbol{\kappa_{\mathbf{f}}}$	Fracture permeability (tensor)
κ_{f}	Fracture permeability (scalar)
κ_{f0}	Fracture permeability in the unstressed state
μ	Viscosity of water
ρ	Density of water
$\boldsymbol{\sigma}$	Stress (tensor)
ϕ	Strike
$\phi_{\sigma 1}$	Angle of the first principal stress
b	Fracture aperture
E	Young's modulus
$\boldsymbol{K}$	Hydraulic conductivity (tensor)
K	Hydraulic conductivity (scalar)
n	Porosity
P	Pressure
s	Fracture spacing
T_{n}	Normal component of surface traction
T_{t}	Tangential component of surface traction
$\mathbf{u}$	Deformation
$\mathbf{v}$	Velocity

Abbreviations

BIPS	Borehole Image Processing System
DFN	Discrete Fracture Network
HRL	Hard Rock Laboratory
REV	Representative Element Volume
TASD	A tunnel intersecting TASO
TASO	Tunnel, where the experiments take place

1 Introduction

The current plan for the management of spent nuclear fuel both in Finland and in Sweden is a deep underground repository system. The repository consists of several engineered barriers to prevent and delay the release of radionuclides, but the final barrier is the bedrock. The bedrock in the Fennoscandian field is old, hard, dense, extensively fractured, and saturated with water. The bedrock at the disposal depth is also under significant loading due to the weight of the overlying rock and tectonic movements.

During the long time span of the final disposal, the stress state of the bedrock will change. The excavations and filling cause changes in the stress state during the operation of the repository. Post-closure equilibration, including the swelling of bentonite, affects the stress field and over a longer time span tectonic movements or an overlying glacier might cause large changes. The stress state affects the permeabilities of rock and rock fractures, which are important to the safety assessment of a deep rock depository as they affect, for example, the wetting of the bentonite and radionuclide transport in the rock. Another research field that has interest in the subject is the petroleum industry [1], where the theory of permeability of a stressed medium is applied to reach the large amount of gas trapped in relatively impermeable sandstone reservoirs.

The Precambrian rock in the Fennoscandian field, and thus the very bedrock of the repository, is saturated with fractures of varying size and orientation due to a long and complicated deformation history. The deformations are a result of large stresses in the rock that also have varied throughout geological history. In Europe and North Africa, horizontal north-west trending first principal stress is typical due to tectonic movements. On a smaller scale, different stress regimes can be observed. A correlation between the orientation of the first principal stress and the orientations of the flowing structures has been reported [2, 3], which show that the best flowing structures can be found parallel to the first principal stress.

The effects of the bedrock structure and permeability properties on the groundwater flow have been studied to a great extent since the early 20th century. The basis of permeability lies in the micro-structure of the rock. Rock mass is a porous material that consists of grains of mineral, packed in a lattice, but also of fractures, which can be found at all scales down to the size of the mineral structure. For modelling purposes, some lower limit for fracture size, depending on the geometry, must usually be determined. Thus, the bedrock is thought to consist of rock mass and fractures that both contribute to the flow. Flow in the fractures is normally faster than in the rock itself, and the differences in permeability of rock and fractures can be many orders of magnitude.

In this study, the relation between bedrock stress and permeability is applied to a model of an in situ experiment. The dependency of permeability on the stress state has previously been widely studied by using experiments, analytical models, and simulations. The research focus has recently been on numerical modelling on simulated data [4, 5, 6, 7] with significant advances, but less has been done in the pursuit of application to in situ bedrock systems. In the present study, an

in situ experiment is modelled directly by using the measured fracture geometry parameters, not by the conventional stochastic discrete fracture network (DFN) model. The stress effect to the permeability of the rock mass and the fractures is computed with different reported relations, instead of assuming the mechanical and hydraulic apertures to be equal, as is commonly done in DFN simulations.

Different models between the stress state and permeability in rock and discrete fractures are reviewed and developed further in this Thesis. A selection of relations from previous studies is chosen for simulations, in addition to constant permeability models. Also, a new empirical model for the fracture permeability is developed, and the selected models are modified to suit the implementation. The relations chosen for simulations should be simple enough to be used in large 3-D simulations, with as little required initial data as possible, and they should still give reasonably accurate results.

The data used in this study was provided by the Bentonite Rock Interaction Experiment (BRIE), which was conducted in the Äspö Hard Rock Laboratory. The model geometry follows the experimental setup of BRIE and is constructed based on fracture data measured at the site. The stress state in the modelling volume is computed based on the known average principal stresses in Äspö. Hydraulic simulations follow the configuration of the experiments, and the measurement results are compared with the simulation results within the limits of the given accuracy. The aim of this study is to test if the stress dependent permeability models could be used to predict the fluid flow measured in the area, and also to study the effects of the stress state on the outcome of the simulations.

In the following chapter 2 the history and development of the rock and fracture permeability models are reviewed. The formulations of the mechanical and hydraulic problem solved in the simulations are presented in chapter 3. In chapter 4 the selected fracture permeability models are introduced, some developments are made and a new permeability model is presented. The rock permeability models are presented in chapter 5, and final selections and modifications are made. Chapter 6 goes through the geometry, setup, phases of the experiments, and the implication of the model. The obtained simulation results with different permeability models are viewed in chapter 7. The results and the model implementation are discussed in chapter 8. Chapter 9 concludes the essential content of the study.

2 Background

In the following sections, the history and development of the research of elasticity and permeability for both rock mass and fractures are introduced.

2.1 Rock modelling

Deep rock reservoirs are saturated with water and under tension. The stress state consists of the confining stress of the upper rock mass and horizontal stresses depending on the tectonics of the area. Stress has an effect on the micro-structure of the rock, and thus, to rock permeability and the flow properties. The theoretical study of poroelasticity, *i.e.*, the theory of the elastic behaviour of porous materials started out for soils. A pioneer work by Biot in [8] presents the basic theory of soil consolidation. The later developments in the field are commonly also applied for granular rock masses.

The research of flow in granular structures started by applying Poisseuille's law for circular channels, when studying flow through granular beds. An empirical formula by Hazen to predict the permeability of loose uniform sized sand [9] was for a long time widely used for in situ soil permeability estimation. Kozeny [10] and later Carman [11] studied the flow of water through granular materials and summarized previous results of the field. They propose a semiempirical, semitheoretical relation for the pressure drop of a fluid through a granular bed, derived from the Darcy's law. Kozeny–Carman equation is more accurate than Hazen–formula [9], but requires information on the grain shape and size distribution.

There are numerous experimental studies on the stress effect on rock, and especially sand, permeability, see, *e.g.*, [12, 13]. The theoretical study of porous media flow from the granular point of view has been further developed by taking the stress state of the material into account. Gangi, among others, presents a model for rock permeability variation under pressure [14]. He makes an assumption that porous rock consists of uniformly sized spherical grains packed in a triangular 2-D lattice, and the grains compress according to Hertzian contact theory when uniform pressure is applied. Flow takes place in the pores between the grains, and the decrease in permeability is due to the decrease in pore size when the rock compresses.

The idea of spherical grains in a lattice under compression was later further developed by Bai and Elsworth. In their model, which is explained in detail in [15], a simple cubic grain packing is assumed, and the change in the permeability is proposed to result from the variation of the mean grain size instead of pores. The pore pressure and the confining stress are combined to form effective stress, for simplicity. A further work by Bai *et al.* [16] presents conceptual models for the permeability of fractured media, intact porous media and fractured porous media. The porous media model is the same as presented in [15]. These models assume uniform compression and no shear effects, and thus cannot explain any effects due to anisotropies.

Other ways to approach the permeability of a stressed rock mass are for example the one presented by Kim and Parizek in [17], where Kozeny–Carman equation

is applied to a rock model. In this model, rock is assumed to consist of a solid rock skeleton, instead of individual grains, and the skeleton compresses under stress instead of individual grains. The essential difference to other models is that the solid volume does not change. The model is isotropic, assumes no shear stresses and that the Kozeny-Carman equation is valid, and on the upside it is mathematically simple.

The aforementioned granular models are widely applied for sandstone and other relatively soft rock materials. The rock deep in the Scandinavian crust, however, is hard and fractured in every scale. A popular and more suitable way to approach the permeability of an extensively fractured bedrock is to assume that it consists of the permeability of uniformly distributed parallel fracture planes. Such models are presented for example in [16]. The behaviour of grains under compression is left out, and all focus is on the behaviour of fractures. The rock between the fracture planes is assumed to be impermeable, and in some models also completely rigid.

2.2 Fracture modelling

In fracture flow, the simplest approximation is the parallel plate model that was first derived from the Navier-Stokes' equations in the 19th century by Boussinesq [18]. The equation is valid for laminar flow through smooth, open fractures consisting of parallel planar plates. Later, extensive laboratory tests, such as by [19, 20] or later [21, 22], show that fracture permeability is proportional to the third power of the fracture hydraulic aperture. This leads to the extensively used cubic law, which forms the basis for basically all fracture permeability equations today. Its validity was first thoroughly studied in [22], and the cubic law was found to be valid for fractures under stress and in contact, and permeability was found to be uniquely defined by the fracture hydraulic aperture. Geometrical deviations from the parallel plate assumption were found to affect the equation only by a coefficient close to one in value. It has since been studied extensively, the key questions being surface roughness, closure and high Reynolds number effects.

In real fractures, the value of aperture depends on the compression of the fracture. The elastic deformation of single asperities can be calculated from Hertzian theory of elastic deformation. One of the first theoretical calculations for the contact of a nominally flat surface was by Greenwood and Williamson in [23]. They study theoretically elastic and plastic deformation of asperities when compressing surfaces. Witherspoon and Gale have written quite an extensive review of the work done thus far in [24]. Work on the asperity distributions in rock fractures and their compression is presented by Gangi and Swan in [14] and [25]. Slightly different conceptual approaches both result in a permeability equation dependent on the applied load. The choice of asperity distribution has a major effect on the relation, both use power law and Swan also exponential and normal distributions. An empirical, cubic-law based equation for the permeability of fractures under normal pressure, along with experimental studies, has been proposed by Gale in [26]. All three relations require few parameters to describe the fracture.

The experimental work on single fractures has been extensive. The anisotropy to the flow caused by shearing is an interesting question, and in the interest of several research fields. Yeo *et al.* [27] and Gentier *et al.* [28], among others, both performed flow tests with a single fracture replica, of sandstone and granite respectively. Yeo *et al.* performed unidirectional tests under constant normal stress and various shear displacements, whereas Gentier *et al.* present results for three shear directions in one directional flow. Both results give indication that the permeability is slightly larger in the direction perpendicular to the shear.

Lee and Cho in [29] performed combined hydraulic and mechanical laboratory tests with artificial fractures in granite and marble. The topography of the fracture was measured using a 3-D laser profilometer. The effects of normal stress and also shear stress and dilation under small normal stress were studied. The flow was laminar and in the direction of the shear. Models presented in earlier studies [14, 25, 26] are compared to the results, and exhibit a high degree of fitness, when applied with suitable parameters. The relation between hydraulic and mechanical aperture is discussed, for example, in [30].

In the development of the analytical models for permeability, shear stress has been taken into account relatively recently, as older models only include normal stress. Now, however, several writers have taken the task. For example, Zhou *et al.* have presented an analytical model to describe the effect of a general stress state on flow [5]. Fractures are modelled as interfacial layers, with no displacement to other than the perpendicular direction, assuming the mechanical response can be described by a linearly-elastic model. The weakness of this model is that it requires a lot of parameters that have to be determined in extensive laboratory experiments, and as such the model has little use in field studies. Shear stress effect in 2-D simulated fracture system is studied by Min *et al.* [31], and an empirical equation between stress and permeability is introduced, based on discrete fracture modelling. The problem in this relation is the same as in the previous one, a lot of parameters need to be determined before any simulations can be made.

The rapidly increasing computational capacity has affected the field, and a majority of the studies from the 21st century are numerical simulations. The DFN method is now common, with emphasis on determining the representative element volume (REV). In the discrete fracture method, the rock consists of a fracture network with similar average properties as the rock under investigation. The problem of determining the permeability tensor is passed over by calculating the mechanical changes, primarily the aperture change, induced by stress, as accurately as possible. Then the flow, which is assumed to take place in the fractures only, can be calculated with the cubic law. This transfers the problem of determining permeability into a problem of presenting the geometry change as accurately as possible. Issues remain though, for example the hydraulic aperture used in cubic law is not the mechanical aperture, and some relation to link them should be used, and also some model between normal stress and normal closure should be applied. Commonly the fracture shear stress–displacement behaviour is modelled with Mohr–Coulombs law [32], and dilation occurs according to a certain dilation angle. The stiffness behaviour and friction angles of the fractures are required.

In a recent study [7], Zhao *et al.* present combined structural, hydraulic and transport modelling by the discrete element method and particle tracing. The stress state is found to be a significant factor in the solute residence time and travel paths. The model uses many simplifications, among the most important are that fractures are smooth and follow the cubic law, and the hydraulic apertures are equal to mechanical apertures with constant initial aperture value for the whole geometry. The simulation is conducted in 2D. Effort has been made to make it from 2D to realistic 3-D geometries. Zhang *et al.* [33] present both numeric calculations and experimental results with the purpose to achieve a stress–permeability relation to work in 3D. A fracture lattice system is applied to be the rock model, with no shearing effects included. Existing results are summarised, and the cubic law is found to be valid.

Fracture permeability and its behaviour under stress is an active field of study, where significant advances, especially in single fracture flow, has been made. In rock permeability, focus has been on the granular approach, but numerical studies of fracture networks are increasing in efficiency and volume.

3 Theory

The computations consist of two parts, the mechanical problem and the hydraulic problem. The mechanical problem is solved before the hydraulic one since permeability in the hydraulic problem depends on the solution of the mechanical problem. Both problems are stationary. Temperature is assumed constant, and the effects of salinity have been neglected for simplicity.

3.1 Structural mechanics

In order to study the effect of stress state to flow properties of rock, the stress field has to be calculated. The principal stresses of the Äspö area in the investigation depth are known and used as initial values for the calculation. The tunnel inner boundaries are set to move freely, and the effect of the investigation tunnel is computed. The outer boundaries of the simulation area are set to have zero displacement, since the boundaries are a part of the bedrock.

From the structural point of view, the bedrock is assumed to be a homogeneous and isotropic material. Fractures are included as surfaces, and the displacements are assumed continuous across them. This is a simplification, in reality fractures are somewhat elastic. Computing them as compressive is possible, but it would require knowledge on the normal and shear stiffness, and their behaviour against stress magnitude. With no such information at hand, continuity is assumed.

The stress $\boldsymbol{\sigma}$ is solved from

$$-\nabla \cdot \boldsymbol{\sigma} = \mathbf{F}_{\mathrm{V}}, \tag{1}$$

where $\mathbf{F}_{\mathrm{V}}$ is the force per unit volume. Hooke's law [34] relates the stress tensor to the strain tensor with the assumption of a linear elastic material

$$\boldsymbol{\sigma} = \boldsymbol{\sigma_0} + \mathbb{C} : (\boldsymbol{\varepsilon} - \boldsymbol{\varepsilon_0}), \tag{2}$$

where $\mathbb{C}$ is the elasticity tensor, $\boldsymbol{\varepsilon}$ the strain, and $\boldsymbol{\sigma_0}$ and $\boldsymbol{\varepsilon_0}$ are the initial stress and strain. For a linearly elastic material the strain is

$$\boldsymbol{\varepsilon} = \frac{1}{2}\left[(\nabla \mathbf{u})^{\mathrm{T}} + \nabla \mathbf{u}\right]. \tag{3}$$

3.2 Hydraulic problem

The physical hydraulic problem is quite straightforward. The computation domain is a cube of bedrock, with certain pressure boundary conditions that are obtained from a larger site-specific model. Inside the rock of the calculation domain are tunnels and boreholes, which have an atmospheric pressure boundary condition. The bedrock has fractures, which have their own, larger permeability. The rock is assumed fully saturated in the whole geometry. The flow in the rock follows the mass balance equation

$$\nabla \cdot (\rho \mathbf{v}) = Q, \tag{4}$$

where the velocity is obtained from Darcy's law

$$\mathbf{v} = -\frac{\boldsymbol{\kappa}}{\mu}\nabla P. \tag{5}$$

Q is a source term, $\boldsymbol{\kappa}$ is the rock permeability for water and μ water viscosity.

In the fractures, a similar tangential mass balance equation prevails

$$\nabla_T \cdot (b\rho\mathbf{v}) = bQ, \tag{6}$$

and velocity follows Darcy's law also in the fractures

$$\mathbf{v} = -\frac{\boldsymbol{\kappa}_\mathbf{f}}{\mu}\nabla_T P. \tag{7}$$

∇_T is the gradient operator on the surface representing the fracture, b is the aperture of the fracture, and $\boldsymbol{\kappa}_\mathbf{f}$ the permeability of the fracture.

4 Fracture permeability models

In rock fracture flow, the cubic law dependence between permeability and aperture is widely used. It is found to work also on fractures under loading. Cubic law is based on a parallel plate model, by far the simplest assumption, yet it does not describe the details of natural fractures. A natural fracture has contact areas, surface roughness and a large variance in aperture [35]. When normal stress is applied, the contact area increases, and average aperture decreases non-linearly.

The difficulty in modelling fractures under load is that some assumption must always be made of the fracture geometry. The effect of shear stress is more tricky, because displacement and dilation are dependent on the topography. Depending on the relative position of the top and bottom fracture profiles, the behaviour under shear can be quite different, as FIgure 1 presents. For single fractures the shear stress-displacement behaviour is widely studied, in for example [28] and [29]. Shear stress increases with shear displacement until a peak value of shear stress is reached. In single fracture measurements this point is reached when shear stress exceeds the normal stress. From there on, a plastic region begins, where shear displacement increases with smaller shear stresses, and dilation into the normal direction begins to take place. In terms of permeability it means a rapid increase of several orders of magnitude, which turns into a moderate increase afterwards. The situation in bedrock differs from the single fracture behaviour, since the fractures are not necessarily free to displace or dilate.

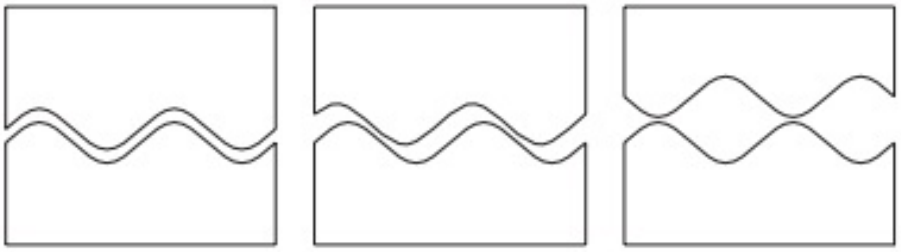

Figure 1: The process of shear can go from right to left or from left to right, depending on the initial mating of the surfaces.

4.1 Bed of Nails model

Gangi presents a model in [14] for fracture permeability that is based on the aperture distribution in a fracture. The model is called the Bed of Nails model, since in it the fracture is assumed to consist of planar planes with rods of different lengths attached to them, looking much like an actual bed of nails. The rods are assumed to behave as elastic springs. Therefore, when normal stress is applied to the surfaces, the rods compress and even more rods make contact, hence the resistance of the fracture increases.

The necessary assumptions of the model are that the flow is laminar, and the surface roughness has little effect on the flow, which can be considered as flow

between smooth parallel plates. Also, the angles of the fracture surface relative to a smooth surface have to be small, so that the flow length does not differ significantly. The distribution function of the lengths of the "nails" is assumed to follow power law.

The advantage of the Bed of Nails model is that it is flexible to the distribution of aperture, the so-called nails. Swan uses an approach similar to the Bed of Nails model in [25], where the fracture surfaces are assumed to consist of hemispherical peaks sufficiently far from each other to deform independently. Three peak height distributions are considered: power law, exponential distribution and normal distribution. These are based on aperture distribution measurements, also presented in the paper. It is found, as in other studies like [27, 29, 35, 36] that natural aperture distributions follow roughly the normal distribution, although for certain parts of the distribution other fits are also reasonable approximations. Other distribution choices for the model than power law are slightly problematic, normal distribution requires a lot more computing power, as the integrals should be calculated at every step. The exponential distribution works well for small normal loads.

Gangi's Bed of Nails model is essentially the same as Swan's with power law aperture distribution. The model requires as parameters the Young's modulus of the material and the initial fraction of contact surface in the fracture. This fraction is different for all natural fractures, but since the model has to be sufficiently simple and computationally not too heavy, a general value for all fractures must be assessed. The estimate is based on several studies, for example [23, 35], wherein the aperture profiles of bedrock fractures has been measured. The model requires also initial permeability, which is calibrated from in situ experiments.

For the assumed planar fracture, permeability can be calculated from the cubic law

$$\kappa_{\mathrm{f}} = Cb^3. \tag{8}$$

If the permeability at a certain aperture is known, the change in permeability can be calculated from the change of the aperture

$$\kappa_{\mathrm{f}} = \kappa_0 (b/b_0)^3, \tag{9}$$

where b_0 and b are the apertures before and after the application of pressure.

The force required to move the two faces of a fracture closer to each other by a distance x can be expressed as

$$F(x) = \sum_{i=1}^{I} k_i n(l_i) R(x - b_0 + l_i), \tag{10}$$

where I is the total number of rod sizes, k_i is the spring constant of the i:th rod, $n(l_i)$ is the number of rods that have length l_i, and $R()$ is a ramp function.

The rods keeping fracture surfaces apart can be considered as springs defined by a spring constant. The stiffness of an ideal spring is expressed as

$$F = -kx, \tag{11}$$

where k is the spring constant and x the distance from the springs' initial length. Then again, Young's modulus is defined as tensile stress per tensile strain. This is

$$E = \frac{\sigma}{\varepsilon} = \frac{F/A_0}{\Delta L/L_0}, \tag{12}$$

where F is the force exerted on the object, A_0 is the cross-sectional area of the object before application of the force, L_0 the original length and ΔL the change in length. Combining equations (11) and (12) we get

$$k = \frac{EA_0}{L_0}. \tag{13}$$

For all rods in the Bed of Nails system, it is similarly valid that

$$\frac{a_i}{l_i} = \frac{k}{E} = \text{constant} = \beta b_0, \tag{14}$$

where a_i is the cross-sectional area of each rod and $\beta << 1$, is a constant chosen for simplicity. From now on all the rods are assumed to have the same spring constant k for simplicity.

The pressure that is exerted on the faces of the fracture can be calculated from the definition of pressure using equations (10) and (14)

$$P(x) = \frac{F(x)}{A} = \frac{E\beta b_0}{A} \sum_{i=1}^{I} n(l_i) R(x - b_0 + l_i), \tag{15}$$

where A is the fracture area. From now on the "shortness" of a rod $\xi_i = b_0 - l_i$ is used as the variable, for simplicity. The summation is convenient to turn into an integral of the distribution function over the shortnesses $dN(\xi) = n(\xi)d\xi$, where $N(\xi)$ is the distribution function of the shortnesses of the rods.

$$P(x) = \frac{E\beta b_0}{A} \int_0^x (x - \xi) n(\xi) d\xi. \tag{16}$$

The distribution function $N(\xi)$ depends on the geometry of the fracture, but some function must be chosen to represent it. The recorded aperture distributions form approximately a Gaussian curve, and thus their distribution function is the error function. Gangi has chosen power law as the distribution function of the Bed of Nails model. This makes sense, as linear power law, *e.g.* exponent 2 is a good approximation of the central part of the error function in many cases. The distribution function is then of the form

$$N(x) = I_0 \left(\frac{x}{b_0} \right)^{n-1}. \tag{17}$$

Now the integral can be calculated.

The pressure exerted on the faces of the fracture takes now the form

$$P(x) = \frac{E\beta b_0^2 I_0}{nA} \frac{x}{b_0}^n . \tag{18}$$

As $x = b_0 - b$, we get

$$\frac{b}{b_0} = 1 - \left(\frac{P}{P_1}\right)^{\frac{1}{n}}, \tag{19}$$

where $P_1 = E\beta b_0^2 I_0 / nA$. The area covered by rods at b_0 is

$$A_r = \int_{N(0)}^{N(b_0)} a(\xi) dN(\xi) = I_0 \beta \frac{b_0^2}{n}, \tag{20}$$

which leads to

$$P_1 = E\frac{A_r}{A}. \tag{21}$$

Uniting equations (9), (19) and (21) and remembering that $n = 2$ was chosen, the final formulation of permeability according to the Bed of Nails model is

$$\kappa_\mathrm{f} = \kappa_0 \left(1 - \left(\frac{P}{P_1}\right)^{\frac{1}{2}}\right)^3 . \tag{22}$$

4.2 Exponential model

Min *et al.* in [31] have derived a model for the permeability of fracture sets as a function of stress state in 2D. The model is experimental, based on a discrete fracture network study. The behaviour of single fractures in the network is calculated, and the general permeability behaviour of a fracture network is studied. A number of simulations at different stress conditions are run, and an analytical equation is fitted to those simulation results. In the simulations, a stepwise linear model for normal stiffness of fractures and a constant shear stiffness are used. Stiffness is the slope of a stress–displacement curve. The rock blocks between fractures are assumed continuous, homogeneous, isotropic, linearly elastic and impermeable. The shear stress–shear displacement fracture behaviour is modelled by an elasto-perfectly plastic constitutive model with a Mohr-Coulomb failure criterion [32], where dilation takes place in the plastic region.

The analytical model is derived to fit the described simulation results. Both normal and shear effects are included, their permeabilities in each direction are calculated independently, and it is assumed that the sum of shear and normal permeability gives the total directional permeability. The cubic law is used for the relation between permeability and hydraulic aperture. The permeabilities are not for single fractures but for fracture systems of a specified fracture density.

The difference between this model and most of the others is that it is an empirical model and thus takes no notion of the micro-structural theory of fracture surfaces.

This model is slightly modified for the purpose of this study. Instead of taking the total permeability as the sum of normal and dilational permeabilities, it is assumed that the aperture is the sum of the dilation and the aperture that deforms due to normal stress. The cubic law is used to get the permeability from the total aperture. With these changes the permeability is taken as a representative permeability for a single fracture in bedrock, not a fracture set permeability.

It is proposed that an aperture under normal loading can be divided into two parts, the deformable aperture and the residual aperture [22]. As the normal loading increases, the deformable aperture decreases and the total aperture approaches the residual aperture. The form of the normal stress to aperture curve is known [24], so the normal stress-dependent aperture can be assumed to take the form

$$b = b_{\mathrm{res}} + b_{\max} \exp(-\gamma_1 \sigma), \tag{23}$$

where γ_1 is a parameter related to the curvature of the exponential function.

The shape of shear stress–displacement curve is different when the normal displacement is restricted. Dilation forms a first rapidly increasing and later slowly increasing curve against shear displacement, and no peak nor elastic region forms [24]. In an unlimited case, shear dilation takes place after the ratio of shear to normal stress exceeds a threshold k_{c}. If the friction angle of the fractures is known, the value of the threshold can be calculated from the Coulomb failure criterion [32]

$$k_{\mathrm{c}} = \frac{1 + \sin \Phi}{1 - \sin \Phi}, \tag{24}$$

where Φ is the friction angle of the fractures. The shear dilation term is

$$d = d_{\max} \left[1 - \exp(-\gamma_2(\eta - k_{\mathrm{c}}))\right], \tag{25}$$

where $d_{\max}$ is the maximum possible dilation in the fracture and γ_2 the curvature of the dilation function. The equation is only valid when $\eta - k_{\mathrm{c}} > 0$. Experiments for free single fractures [28, 29] suggest that when the ratio is approximately 1, dilation begins to take place, indicating that the friction angles are very small. In bedrock, where the fractures are within the rock matrix, the situation is not as simple. Large DFN-simulations suggest that the threshold in fracture systems is larger, 3 according to [7] and [31]. The ratio increases when fractures are not free to move, and the elastic region may not be reached. As the fractures are in old bedrock that has a complicated stress field history, some fractures might be past the threshold and have already dilated and are in the elastic region, thus having a significantly decreased shear stress.

If the aforementioned difficulties are neglected, the equation form of dilation can be expressed as

$$\kappa = \left(b_1 + b_2 \exp(-\gamma_1 |T_n|) + (b_2 - b_1) \left(1 - \exp\left(-\gamma_2 (|\frac{T_t}{T_n}| - 1) \right) \right) \right)^3, \tag{26}$$

where b_1 is the residual aperture, b_2 is half of the maximum aperture, T_{t} is the tangential component of the surface traction and T_{n} is the normal component of

the surface traction. As with the original model, [31], the problem with Eq. (26) is the numerous parameters that have to be determined. The γ_1 and γ_2 values were chosen to yield somewhat credible shapes. Influence was taken from the curves presented in [22, 26, 28] and [29]. The aperture change was chosen to be three orders of magnitude, and the values of residual and the half maximum aperture were calibrated. The model bares no other distinction of direction than normal to and along the fracture plane in question.

4.3 Angular model

A completely new model is presented here, based on the experimental results reported in [2]. In the paper, orientations of recorded wet fracture sets from Äspö HRL area are compared to the principal stress directions of the region. It seems that most of the wet fractures belong to a set parallel to the first principal stress, the direction most prone to shearing and dilation, and with least normal stress. Also, the direction with least wet structures is parallel to the third principal stress. These both apply for subvertical fractures. In subhorizontal direction, there are also some reported flowing structures, although less than in the vertical direction.

Based on this information, an equation is derived, where the permeability of a fracture depends solely on its direction in respect to principal stresses. In the direction of the strike, permeability reaches its maximum when it is perpendicular to the first principal stress. When considering dip, the permeability reaches its significantly smaller peak value when the dip is close to 0 or 90 degrees. Based on no other information we can formulate

$$\kappa_{\mathrm{f}} = \kappa_{\mathrm{min}} + \kappa_0 \frac{1}{6} \left(\kappa_{\mathrm{dip}} + 2\kappa_{\mathrm{strike}} + 3 \right), \tag{27}$$

where

$$\kappa_{\mathrm{dip}} = \cos(4\theta) \tag{28}$$

and

$$\kappa_{\mathrm{strike}} = -\cos(2\left(\phi_{\sigma 1} - \phi\right)). \tag{29}$$

θ is the dip, defined downwards from horizontal plane, $\phi_{\sigma 1}$ is the angle of the first principal stress and ϕ is the strike, defined clockwise from north.

5 Rock permeability models

In models, bedrock is assumed to consist of a rock mass and fractures within. The rock mass can be considered to consist of mineral grains in a lattice, but is often assumed to be a homogeneous mass. The flow in the rock takes place in the space between the grains, the so called pore space. If stress causes a change in the size of this space, the permeability changes. If the pore space is very small and the rock is sufficiently fractured, it is impractical to consider the flow in pores, and one might comprehend the rock permeability as flow in a matrix of uniformly spaced channels in an impermeable medium. The appropriate approach depends on the rock type.

In the granular approach, there are two ways to regard the compression process: either the grains themselves are assumed to compress, which causes the total volume and pore space to change, or only the pore space compresses, while the individual grains are considered relatively incompressible. A similar division concerns also fracture lattice models, wherein the rock blocks between fracture planes can be considered either rigid or elastic.

5.1 Volumetric-strain dependent model

A simple mathematical relation between stress and permeability has been derived by Kim and Parizek in [17]. The objective of the study is to generate a mathematically simple model that is still a significant improvement to a constant rock permeability. In the model, bedrock is not considered as individual grains in a lattice, but as a uniform solid skeleton. The skeleton is assumed elastic, to surround the pore space, and the individual solid grains are assumed relatively incompressible. The model assumes that Darcy's law and Hooke's law are valid and that the mechanical deformation of the skeleton does not alter the shape factor of the Kozeny–Carman equation. The shape factor expresses the effect of the shape of the solid grains on the hydraulic conductivity, and it has to be assumed unchanging during a deformation. For this reason shear stress cannot be included. The main advantage of the model is that the derivation is simple and understandable. It is also fast to compute since it is isotropic and depends only on volumetric strain.

For a porous medium, the change in the porosity n due to the deformation of the solid skeleton can be expressed as

$$dn = d\left(\frac{V_\mathrm{P}}{V_\mathrm{T}}\right) = \frac{dV_\mathrm{P}}{V_\mathrm{T}} - n\frac{dV_\mathrm{T}}{V_\mathrm{T}}, \tag{30}$$

where V_P is the pore volume and V_T is the total volume. In case that the individual grains are incompressible, the solid volume does not change $dV_\mathrm{S} = 0$, and hence $dV_\mathrm{T} = d(V_\mathrm{P} + V_\mathrm{S}) = dV_\mathrm{P}$. Thus Eq. (30) becomes

$$dn = (1 - n)\frac{dV_\mathrm{T}}{V_\mathrm{T}}. \tag{31}$$

Integrating this from the unstressed state gives

$$\frac{1 - n_0}{1 - n} = \frac{V_\mathrm{T}}{V_{\mathrm{T}0}}, \tag{32}$$

where V_{T0} and n_0 are the volume and porosity at the unstressed state. Using the notion $V_T = V_{T0} + \Delta V_T$ and the definition of volumetric strain $\varepsilon_{VOL} = \Delta V_T / V_{T0}$ yields

$$n = 1 - \frac{1 - n_0}{1 + \varepsilon_{VOL}}. \tag{33}$$

Until Eq. (33), the assumptions have been quite reasonable. The next step consists of making the relation between saturated hydraulic conductivity and porosity, by applying the Kozeny–Carman equation [9]

$$K = \frac{\rho_w g}{\mu_w} \kappa = \frac{\rho_w g}{\mu_w} f(s) f(n) d^2, \tag{34}$$

where ρ_w and μ_w are the density and viscosity of water, κ is the intrinsic permeability, $f(n) = n^3/(1-n)^2$ is the porosity factor and $f(s)$ the shape factor. Substituting Eq. (33) into Eq. (34) we get

$$\kappa = \kappa_0 \left[\left(\frac{1}{n_0} \right) (1 + \varepsilon_{VOL})^{2/3} - \left(\frac{1 - n_0}{n_0} \right) (1 + \varepsilon_{VOL})^{-1/3} \right]^3, \tag{35}$$

where κ_0 is the initial permeability before any deformation takes place. Eq. (35) is valid only on the condition that $\varepsilon_{VOL} > -n_0$. A constant value for the permeability is used in modelling for the area where the relation is not valid.

The model is intended as an improvement to using constant rock permeability, and differences in prediction from other numerical and analytical models is reported in [17]. However, the model cannot explain hydraulic anisotropy, often found in rock formations. The limitations of the Kozeny–Carman equation must be kept in mind, since it assumes a reasonably uniform grain size and random pore structure, and thus does not necessarily work for parallel oriented structures.

5.2 Granular models

A widely used way to approach rock permeability is to examine its grain structure. Flow takes place in the pore space between the grains, and when the grains compress, the volume of pore space changes. The grains are assumed spherical, and their compression can be calculated with Hertzian contact theory. Assumptions on grain packing and compression may vary between models. Gangi in [14] presented one equation for permeability of compressing grains in a triangular lattice

$$\kappa = \kappa_0 \left(1 - C \left(\frac{P}{P_0} \right) \right)^4, \tag{36}$$

where

$$P_0 = \frac{4E}{3\pi} \tag{37}$$

is the reference pressure, where E is the Young's modulus. P is the effective pressure in the rock, and C a geometrical parameter that Gangi suggests to be approximately 2 for spherical grains.

Bai and Elsworth presented their slightly altered model for grains in a simple cubic lattice in [15]

$$\kappa = \kappa_0 \left(1 \mp \frac{1}{2} \left[\frac{9\,(1-\mu^2)}{2} \left(\frac{\pi P}{E} \right)^2 \right]^{1/3} \right)^2 . \tag{38}$$

κ_0 is the unstressed permeability and μ the Poisson's ratio. The negative sign refers to compressional loading and the positive sign to dilatational loading. Both models are isotropic and are functions of the effective pressure.

These type of models are frequently used for sandstone applications, but for granite with a Young's modulus as high as 60 GPa, the differences in permeability tend to be small. They both also assume that the pressure is uniform, which is unrealistic in this particular in situ application. Neither of these models were used in the simulations in the end, since they differ only minimally from constant permeability.

5.3 Uniformly spaced fracture lattice

The crystalline granite of Scandinavia is fractured. This is why assuming the rock to consist of an evenly spaced fracture lattice in impermeable rock, is reasonable. The permeability for paralleled fractured rock has been derived long ago [32]

$$\kappa = \frac{1}{12s} b^3, \tag{39}$$

where s is the fracture spacing. In a stress field, however, the fracture apertures cannot be assumed constant, but some model that takes their compression into account should be added. There are many alternatives, stress or strain dependent, like the models presented in the previous section (Fracture permeability models) of this study.

In the fracture lattice model, it is assumed that the rock matrix consists of fracture planes oriented in three perpendicular directions that are assumed to be the principal stress or strain directions. This assumption makes the problem easier, since there is no shearing in this coordinate system. This is not a completely arbitrary choice, since rock tends to crack roughly along the stress directions [32]. Old rock has known different stress states in its geological history, and contains fractures in basically all directions.

In a fracture lattice, flow in one direction is affected by the stress or strain in the other two directions, as the apertures of the fractures change. If all fractures have the same initial aperture and the rock has a uniform fracture spacing, half of the flow in direction 1 is controlled by stress in direction 2 and the other half by stress in direction 3. This situation is illustrated in Figure 2. Thus the effective aperture that transmits flow to direction 1 is the arithmetic mean of the apertures in direction 2 and 3. This approach can be regarded as a simplified arithmetic version of the model presented in [33].

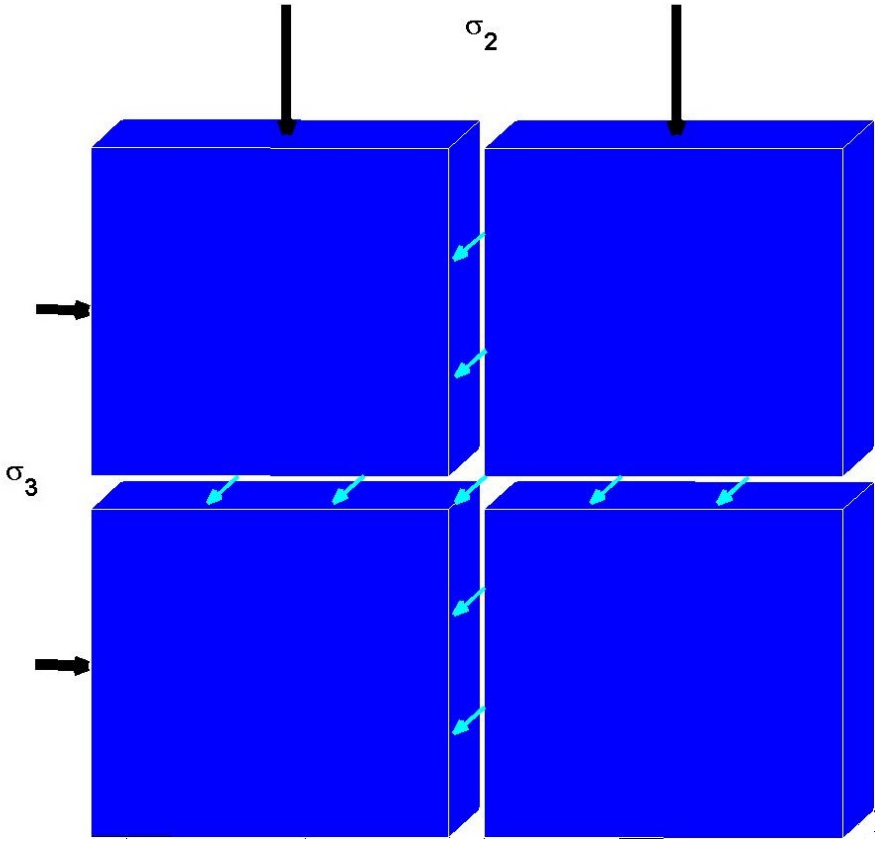

Figure 2: The uniform lattice geometry with flow to direction one (light blue arrows) and controlling stresses (σ_2 and σ_3) to directions 2 and 3.

5.3.1 Bai model

The first simple model used was presented as a 2-D version by Bai *et al.* [16]. In the equation it is assumed that the fractures are soft in respect to the rock matrix, so that the strains are only a result of the displacement of the fractures, the rock does not deform. The bedrock permeability in one direction can thus be expressed as

$$\kappa_j = \frac{1}{12s}\left(b_0 + \frac{s}{2}\left(\sum_{i\neq j}\varepsilon_i\right)\right)^3, \tag{40}$$

where b_0 is the initial aperture of all the fractures and s the fracture spacing, which is also same in all directions. The permeability needs to always be positive, *e.g.*, the fractures cannot close more than to zero aperture. This gives Eq. (40) a validity condition

$$\sum_{i\neq j}\varepsilon_i \geq -\frac{2b_0}{s}. \tag{41}$$

When the sum of the strains is below the threshold, a constant value for permeability is applied.

This model poses the numerical difficulty that the permeability differences between directions can easily be 10 orders of magnitude, as the sums of the strains computed by the structural model can be up to millimetres. Therefore, limitations are made when applying the relation. It is assumed that the fracture cannot close to zero aperture, but residual aperture behaviour is presented. It is also assumed that the aperture of the fractures cannot increase infinitely, but that there is a maximum aperture, after which further increase in strain does not increase permeability any further . This is not in line with the basic idea of the model, but numerically necessary. The sharpness of the edges is slightly smoothed to make the first derivative continuous.

5.3.2 Gangi model

The constant aperture in Eq. (39) can be modelled also by other means. One choice would be to use some fracture model, like the Bed of Nails model presented by Gangi(Eq. (22)). In a uniform fracture lattice coordinate system, such as in Figure 2, it would yield

$$\kappa_j = \frac{1}{12s}\left(b_0\left(1 - \frac{\frac{1}{2}(\sum_{i\neq j}\sigma_i)}{P_1}\right)\right)^3, \tag{42}$$

where σ_i and σ_j are the perpendicular normal stresses and P_1 is the parameter of the Bed of Nails model, Eq. (21). The problem here is that the Bed of Nails model is valid only for compressive stresses and the stress gets tensile in some areas close to the tunnel. To simplify the model, it is assumed that the maximum permeability is reached with the initial aperture, *e.g.*, fractures do not expand. Also, only the sign of the sum of the stresses is taken into account. The summation oversimplifies the situation as large stresses of opposite signs compensate each other.

6 Geometry and Modelling

The simulations follow the Bentonite Rock Interaction Experiment (BRIE) conducted in the Äspö Hard Rock Laboratory, which is a well known rock mass in Sweden with an extensive tunnel network. The investigation tunnel in question is called TASO, a side tunnel from a larger one called TASD; both are in the depth of approximately 400 m.

The basic tunnel geometry of Äspö tunnels TASO and intersecting TASD, presented in Figure 3, was imported to COMSOL Multiphysics [37] from a CAD-file representing the site. In the model, north is parallel to the direction of the y-axis. The geometry includes three full-size deposition-holes that are bored to TASD and TASO floors. Three large fracture-zones, *i.e.*, large fracture 1, large fracture 2, and NNW4 have been found in the experiments of the area of interest (Figure 3). These are imported as planar surfaces to the model. Transmissivities and apertures for the fracture-zones have been estimated in previous large scale flow tests [38].

The inflow experiments done in TASO can be divided into two phases based on the geometry. In the first phase, five holes of 76 mm diameter were bored to TASO floor and their fracturing was recorded and flow and pressure experiments were conducted. In the second phase, two of the holes were expanded to 300 mm diameter, ten new holes were bored around the previous ones, and four to the TASO walls. The boreholes have depths varying around 3 m, and the horizontal holes are 10 meters deep.

The holes are indexed according to the following system: 00G00, where the first digits indicate the number of meters the hole is from the start of the tunnel. The first five holes have numbers 14, 15, 17, 18, and 20. The second digits after the letter can be either 01, 02, 03, or 04. The five holes of the first phase are all along the same line and all have secondary digit 01. Holes labelled with 02 are found on a line south–east from the first-phase holes and those with 03 to north-west. The holes labelled with 04 are found along the original line, but always after the 01-hole.

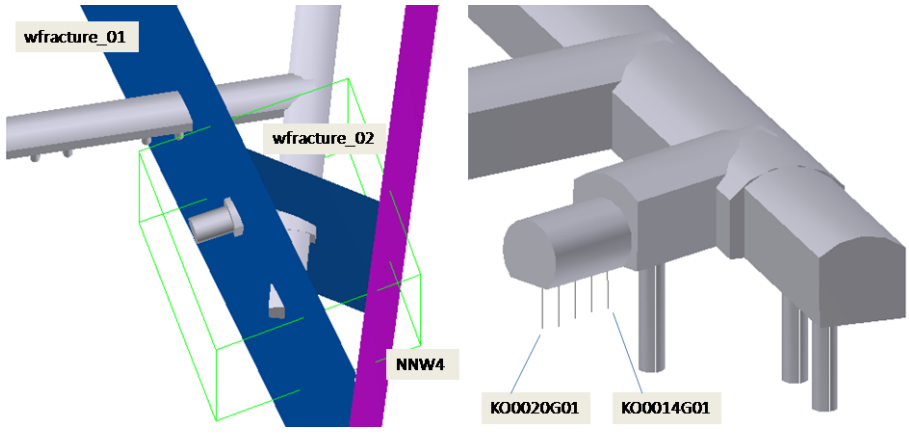

Figure 3: Left: tunnel network, observed large fractures and the outline of the larger cubic model geometry are illustrated. Right: the five first phase boreholes on TASO floor and their indexing is presented [38].

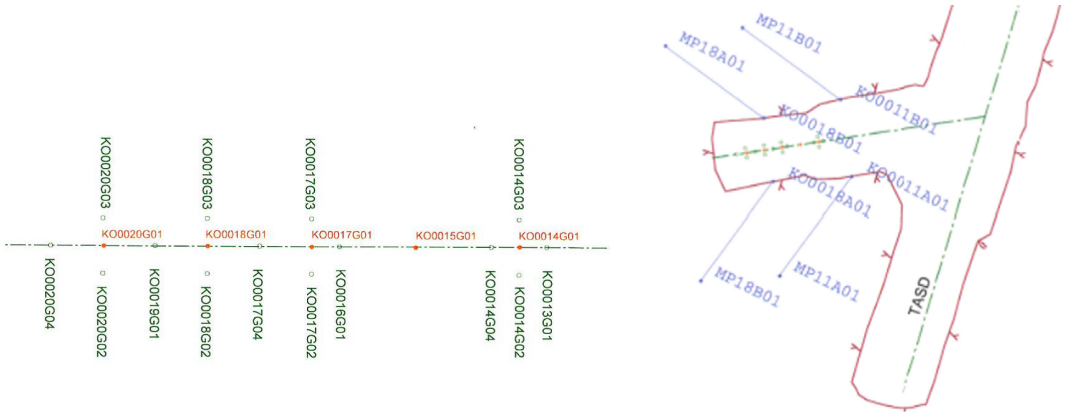

(a) Boreholes in the TASO tunnel floor. (b) Boreholes in the TASO tunnel walls.

Figure 4: Boreholes in TASO tunnel in phase 2 [38].

The horizontal boreholes have letter A on the south side of the tunnel and letter B on the north side. The first and second phase hole-orientation and their indexing is presented in Figure 4.

Core studies and Borehole Image Processing System (BIPS) imaging were done for the five first phase boreholes to study the fracturing. 78 fractures were recorded in total. Such an amount of fractures is impractical for meshing and calculations in COMSOL. The set of fractures had to be reduced by some logical means.

The first basis for reduction was to include only fractures that are observed in the BIPS. This is because BIPS imaging might be easy enough to be used when a repository is in operation, whereas examining cores of every single borehole of the repository could be impractical. Thus, in a real application, only fractures visible in BIPS would be included in the flow calculation.

Secondly, fractures that were reported as confidently sealed were excluded. Also fractures too close to others were eliminated due to meshing difficulties. After these eliminations 31 fractures remained. Creating a mesh to a domain with all these would be impractically time-consuming, and would lead to memory problems because of the heavy computational load. Talbot in [2] shows that in nature, fractures perpendicular to the first principal stress conduct the least water, and that best conductors are fractures subparallel to the first principal stress. Based on this information, fractures perpendicular to the first principal stress, meaning fractures with a strike between 198–218^o or 18–38^o, were excluded. This led to the elimination of three more fractures. Finally, six fractures were eliminated because of their similarity in location and orientation compared with other remaining fractures.

Twenty-two small fractures around the boreholes remained to be included in the geometry. Fractures were assumed planar, and thence were imported as planar surfaces into the model. They were assumed to reach a distance of 0.3 m from the borehole center. There is no practical way of determining the real shape and span of all the fractures, so some approximative assumptions were made. The radius of 0.3 m is an estimate of the fracture length, based on previously reported transmissivity values [38]. In phase two, two more fractures were reported as flowing structures in

boreholes 17G01 and 18G01, and were added to the geometry along with the chosen fractures in phase one.

For necessary water and granite material parameters the COMSOL Material Library values were used, since they are in the range of the measured values in the BRIE area. For the large fracture zones, flow tests have been performed, and estimates for their transmissivities exist [38]. From core tests of rock samples estimates for the rock permeability values have been made.

The fracture aperture values are difficult to determine. Rough estimates on the mechanical apertures were reported with the fracture data that was provided. The mechanical aperture differs from the hydraulic aperture, and the relation is still under research. The cubic law, and thus all the hydraulic models, uses the hydraulic aperture. Since the fracture models are based on the cubic law, and since the cubic law depends on hydraulic aperture, all fracture models are models of aperture deformation as well as permeability. It would, thus, be possible to compute the effect of stress on aperture, and use this deformed aperture value in the computation of the inflow from the fractures, according to Eq. (6). Nevertheless, this was left out of the model and a constant fracture aperture was applied when computing the inflow. This was done in order to get a clear interpretation of the effects the models have on fracture transmissivity. The hydraulic aperture of the large fracture-zones was 10^{-5} m and 10^{-6} m for the small fractures.

The initial rock and fracture permeabilities, κ_0 and κ_{f0}, were calibrated. The water inflow to the TASO tunnel has been both computed based on large scale pressure–distance data, and measured by water–collection tests [38]. The value is 0.5 l/min and the measured value from the sorbing mats 0.1 l/min. The calibration value used was 0.2 l/min for the whole TASO tunnel.

The model built in COMSOL included two Physics Modules, Solid Mechanics and Darcy's Law. The CAD Import Module kernel was used for the geometry, because it was mainly imported from a CAD file, and because great accuracy in small features was required. The default settings of the Solid Mechanics module (quadratic discretization) worked well for the mechanical problem. The default settings of Darcy's Law module are enough for the isotropic rock permeability models. For the diagonal rock permeability models, linear-element discretization was used, because of its ability to follow rapid changes. Permeability and fracture-conductivity models are either inserted directly to the model using the free field or implemented as piecewise functions.

The meshing proved to be sensitive. The difficulty was to create a mesh that suited the geometry with large differences in scale, and the 2-D surfaces in a 3-D geometry. The meshes were built to yield maximum accuracy close to the boreholes, where the measurements take place, with the limitation of required memory. As the structural mechanics computation is more demanding, having three variables to compute instead of just one as in the hydraulic problem, the mesh was significantly more coarse than the mesh of the hydraulic problem.

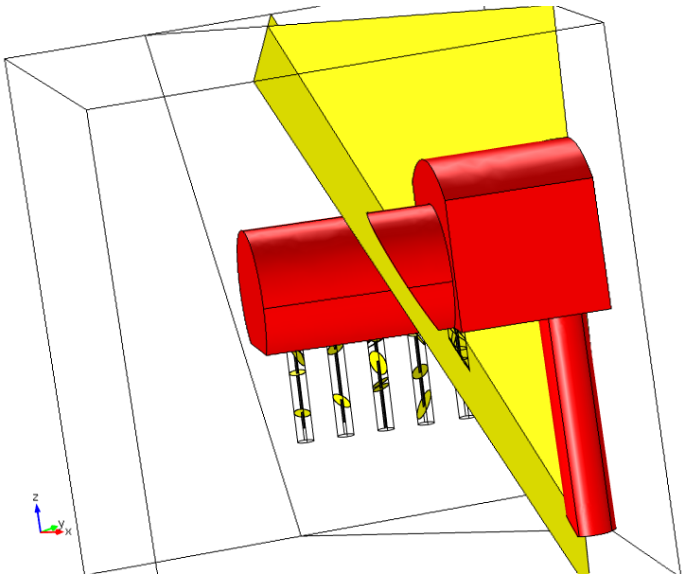

Figure 5: The finalized geometry for simulations in phase one. TASO tunnel with one deposition hole at the start of the tunnel (red), large fractures (yellow) and the boreholes (black) with the surrounding small fractures (yellow).

7 Results

Measurements conducted in the boreholes of Äspö Hard Rock Laboratory were simulated with different models. The stress state of the bedrock was calculated first. The flow simulations can be divided into two phases according to the geometry, as described in the previous section. In the first phase of the experiments there were five boreholes of 7.6 cm diameter on the floor of TASO tunnel. Pressure and inflow measurements were conducted with focus on borehole 17G01. For the second phase, holes 17G01 and 18G01 were expanded to 30 cm diameter and additional 14 holes were drilled around the previous ones. Again, pressure and inflow tests were conducted. All these experiments were simulated using combinations of different models for rock and fracture permeabilities.

During inflow tests, all other holes were sealed, except for the examined one. In the first phase, the total inflow test to the holes succeeded in giving results to only two holes, *i.e.*, 17G01 and 14G01. Inflow to 17G01 was also measured from a depth range of 0.5–2.97 m, in relation to the tunnel floor. In phase two, the flow experiments were conducted on 17G01 and 18G01, and pressure measurements on selected new holes. The inflow to TASO tunnel floor was also measured.

For both bedrock and fracture permeability, the computations were done first with constant permeabilites. In addition for bedrock, *Volumetric* model (Eq. (35)), plain fracture lattice model (Eq. (40)) referred to as *Bai*, and the compressive fracture lattice model (Eq. (42)) referred to as *Gangi*, were used. The models used for fractures were *Bed of Nails* (Eq. (22)), *Exponential* (Eq. (26)), and *Angular* (Eq. (27)). A summary of the model principles is presented in Table 1, and the used model combination indexing is presented in Table 2.

Table 1: Summary of the used models.

Name	Description	Reference
Rock models		
Volumetric	Isotropic model, volumetric-strain-dependent	[17]
Gangi	Fracture lattice model, fractures follow Bed of Nails	[14]
Bai	Fracture lattice model, rigid rock	[15]
Fracture models		
Bed of Nails	Compressing asperity distribution	[14]
Exponential	Derived from a DFN simulation, shear included	[4]
Angular	Empirical model derived based on in situ results	[2]

Table 2: Indexes of the used fracture and bedrock model combinations.

Fracture | Bedrock	*Constant*	*Volumetric*	*Gangi*	*Bai*
Constant	1	5	9	13
Bed of Nails	2	6	10	14
Exponential	3	7	11	15
Angular	4	8	12	16

Table 3: Stress state measured in Äspö.

	σ_1	σ_2	σ_3
Value (MPa)	30	15	10
Angle from North	298	-	208
Angle from horizontal plane	0	90	0

7.1 Stress calculation

The stress state around the investigation tunnel was computed using the general principal stresses of the investigation area as an initial stress state. The measured principal stresses are presented in Table 3. All stresses are compressive, as is normal in deep rock reservoirs. The principal stresses and the effect of the tunnel are illustrated in Figures 6 and 7 respectively.

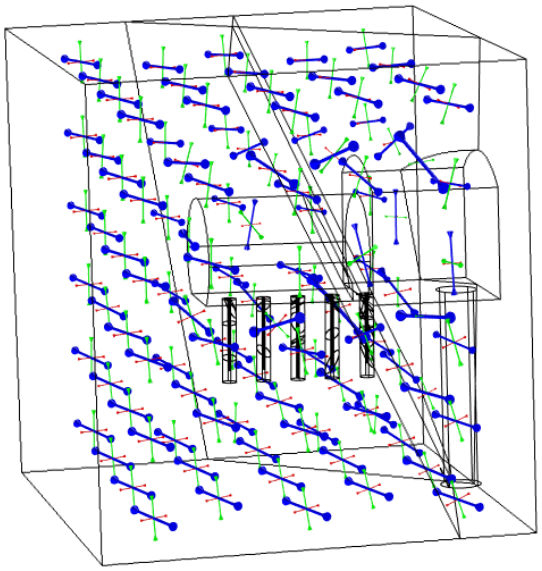

Figure 6: Principal stresses in the model volume.

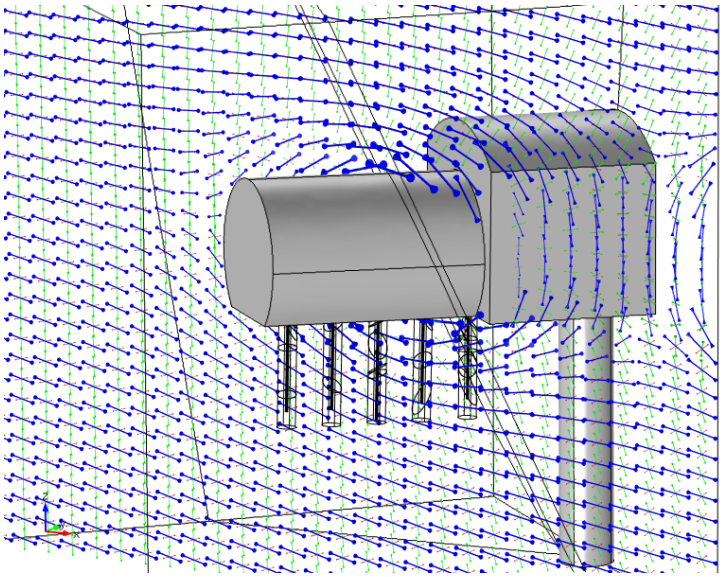

Figure 7: Principal stresses around TASO tunnel.

7.2 Calibration of initial permeabilites

All the models studied have two free parameters that needed calibration: initial bedrock permeability and the initial fracture permeability, initial meaning here the unstressed state. Both parameters were calibrated simultaneously, computing the inflows with different parameter combinations for each model combination. The calibration values were inflow to TASO tunnel 0.21 l/min and inflow in the first phase to borehole 17G01 0.48 ml/min. For the combination 15 this was not reasonably achievable, thus the TASO inflow is 0.22 l/min for that combination. The resulting initial rock permeabilities and hydraulic conductivities of fractures are presented in Table 4, and the parameter values for all models are listed in Table 5.

7.3 Effect of mechanical properties

The dependency of permeability on the mechanical properties could be observed in the permeability profile of the models. Each rock model depends on a different mechanical parameter. The volumetric strain, first principal stress, and first principal strain are presented in Figures 8, 10, and 12 respectively. The corresponding hydraulic model permeability and permeability components are presented in Figures 9, 11, and 13. The permeability value range for *Volumetric* was from 10^{-27} to 10^{-16} m^2. The κ_{XX}-component of *Gangi* permeability ranged approximately from $3{\cdot}10^{-18}$ to $6{\cdot}10^{-18}$ m^2. The κ_{XX}-component of the permeability of *Bai* ranged the predefined 10^{-21} to $5{\cdot}10^{-16}$ m^2.

Table 4: Calibrated values for initial permeabilities and hydraulic conductivities for the used model combinations.

Index	Model		κ_0 (m^2)	K_{f0} (m/s)
1	*Constant*	*Constant*	$3.05{\cdot}10^{-18}$	$6{\cdot}10^{-5}$
2	*Constant*	*Bed of Nails*	$3.2{\cdot}10^{-18}$	$1.95{\cdot}10^{-3}$
3	*Constant*	*Exponential*	$3.35{\cdot}10^{-18}$	$4.8{\cdot}10^{-3}$
4	*Constant*	*Angular*	$3.25{\cdot}10^{-18}$	$4.2{\cdot}10^{-3}$
5	*Volumetric*	*Constant*	$3.1{\cdot}10^{-18}$	$6{\cdot}10^{-5}$
6	*Volumetric*	*Bed of Nails*	$3.25{\cdot}10^{-18}$	$1.95{\cdot}10^{-3}$
7	*Volumetric*	*Exponential*	$3.4{\cdot}10^{-18}$	$4.5{\cdot}10^{-3}$
8	*Volumetric*	*Angular*	$3.3{\cdot}10^{-18}$	$4.1{\cdot}10^{-3}$
9	*Gangi*	*Constant*	$5.58{\cdot}10^{-18}$	$3{\cdot}10^{-3}$
10	*Gangi*	*Bed of Nails*	$5.5{\cdot}10^{-18}$	$2.3{\cdot}10^{-3}$
11	*Gangi*	*Exponential*	$5.83{\cdot}10^{-18}$	$4.7{\cdot}10^{-3}$
12	*Gangi*	*Angular*	$5.67{\cdot}10^{-18}$	$4.8{\cdot}10^{-3}$
13	*Bai*	*Constant*	$1.55{\cdot}10^{-18}$	$3{\cdot}10^{-2}$
14	*Bai*	*Bed of Nails*	$1.54{\cdot}10^{-18}$	$1.6{\cdot}10^{-3}$
15	*Bai*	*Exponential*	$1.76{\cdot}10^{-18}$	$4.4{\cdot}10^{-3}$
16	*Bai*	*Angular*	$1.33{\cdot}10^{-18}$	$3.7{\cdot}10^{-3}$

Table 5: Model parameter values.

Rock models			Fracture models		
Volumetric	n_0	$3{\cdot}10^{-4}$	*Bed of Nails*	A_r	$0.03{\cdot}A$
Gangi	b_0	10^{-6} m	*Exponential*	γ_1	0.03
	s	1/66 m		γ_2	0.1
Bai	b_0	10^{-6} m		b_1	$5{\cdot}10^{-7}$ m
	s	1/16 m		b_2	10^{-4} m
			Angular	K_0	$4.1{\cdot}10^{-3}$ m/s
				K_min	$4.1{\cdot}10^{-6}$ m/s

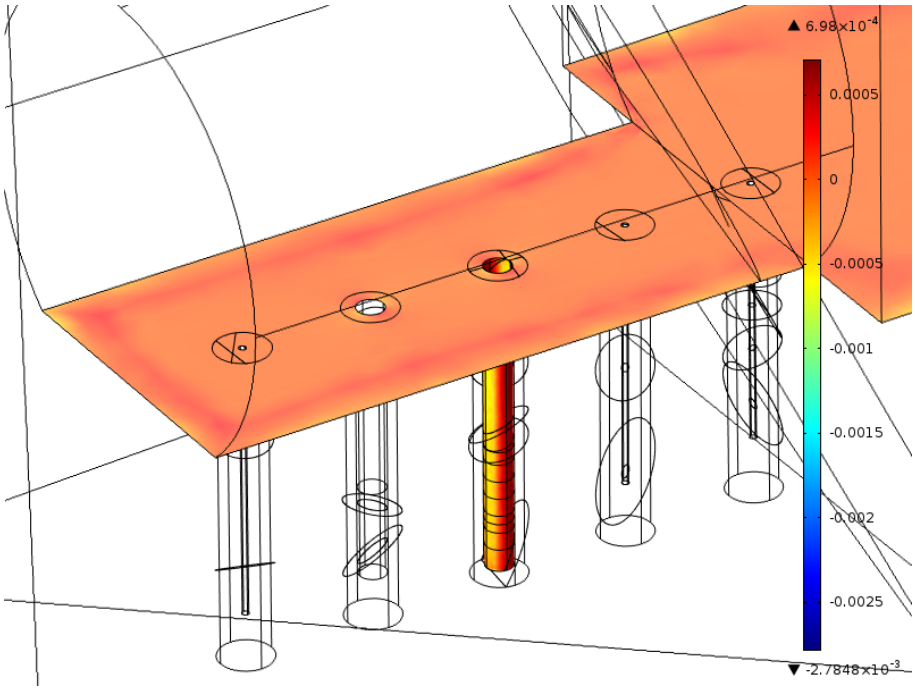

Figure 8: Volumetric strain of the mechanical model on the tunnel floor and borehole 17G01.

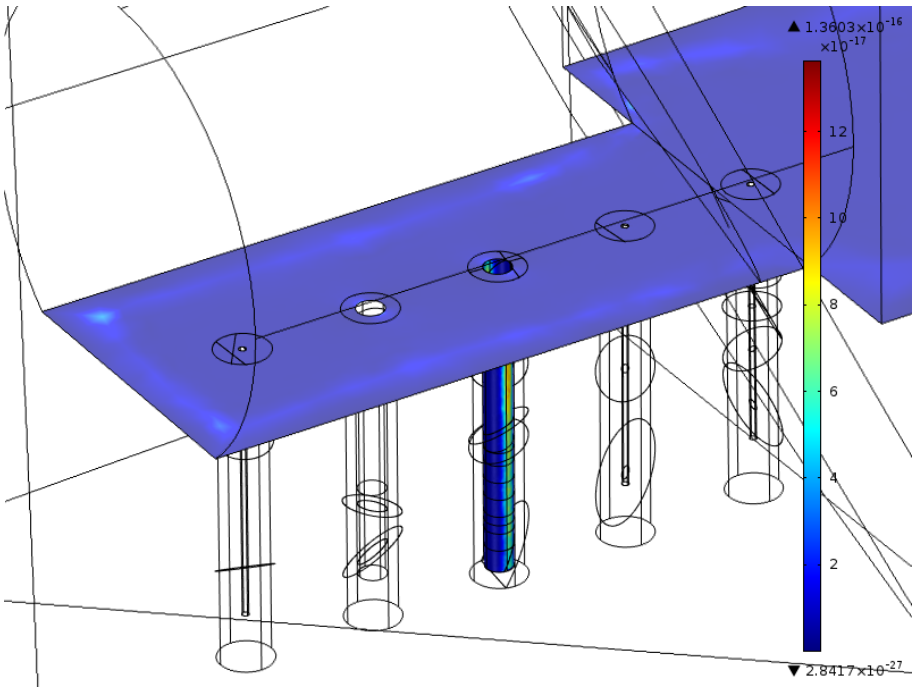

Figure 9: Permeability of *Volumetric* rock model on the tunnel floor and borehole 17G01.

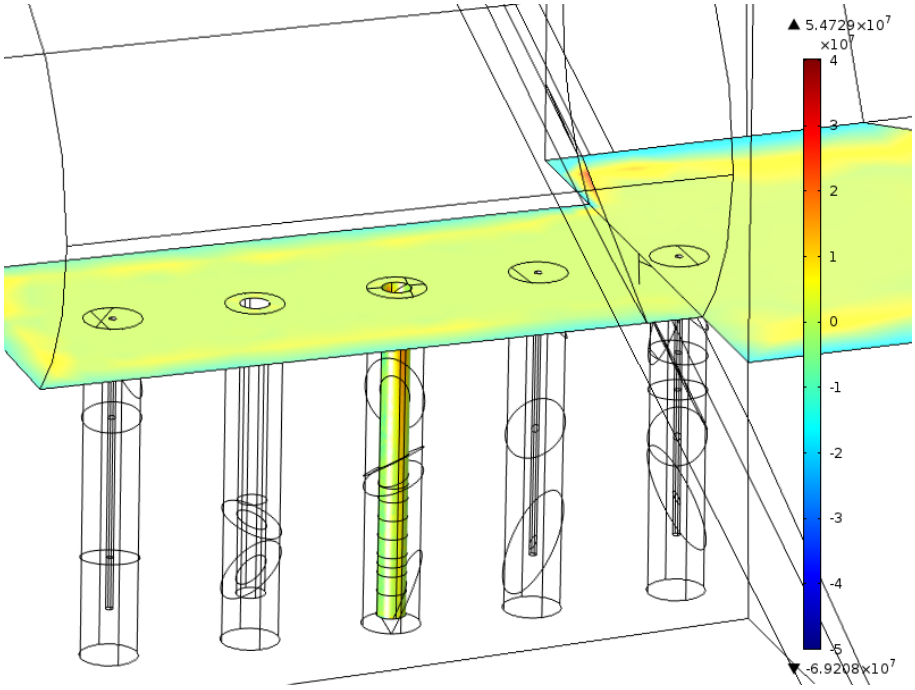

Figure 10: The first principal stress on the tunnel floor and borehole 17G01.

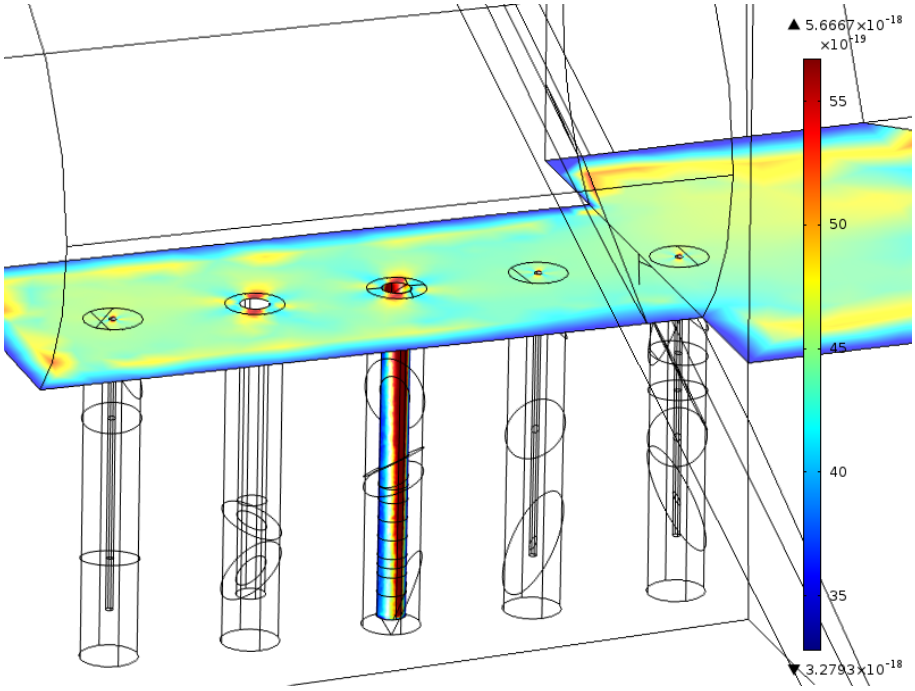

Figure 11: κ_{XX}-component of the permeability of *Gangi* rock model on the tunnel floor and borehole 17G01.

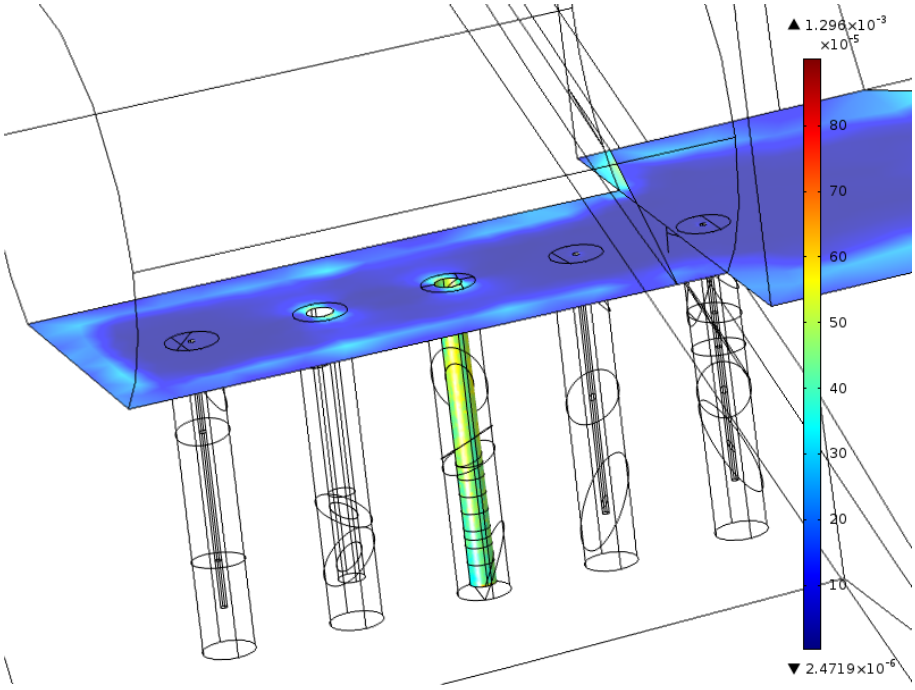

Figure 12: The first principal strain on the tunnel floor and borehole 17G01.

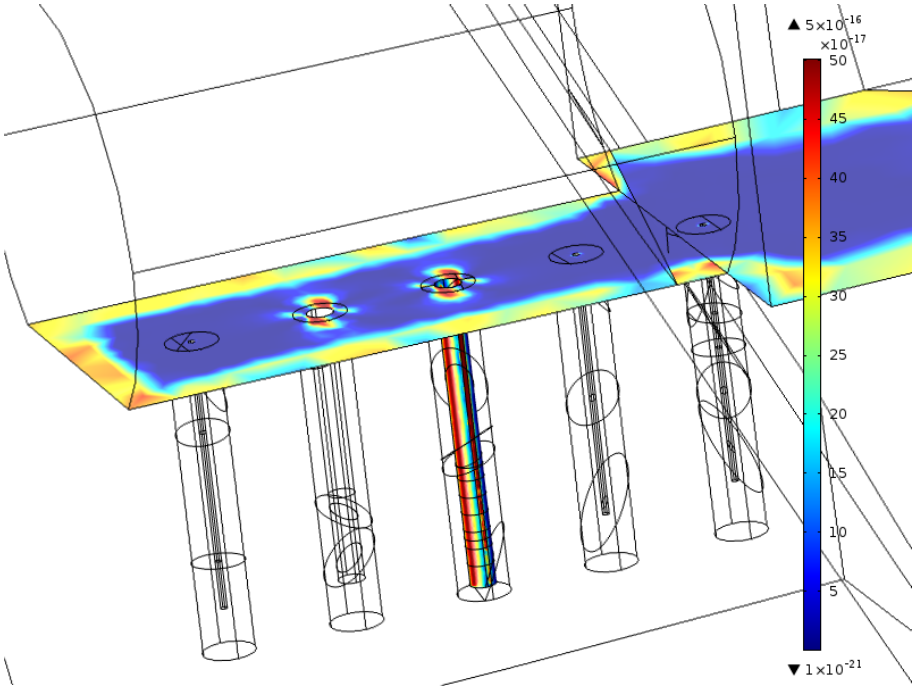

Figure 13: κ_{XX}-component of the permeability of *Bai* rock model on the tunnel floor and borehole 17G01.

7.4 Inflow to borehole 17G01

The inflow to borehole 17G01 has been measured in phase one and with several methods in phase two. The measuring-time interval was 400 min, which is long enough to assume the situation to be stationary.

7.4.1 Inflow in phase one

In phase one the measuring-depth interval of borehole 17G01 was 0.5–2.97 m and the measured inflow was 0.25 ml/min. The calibration inflow value was taken from the entire borehole depth. The inflow from the prescribed depth interval was computed with the different model combinations; the results are presented in Table 6.

The inflows computed with different models ranged from 0.21 to 0.30 ml/min, which are close to the measured value. Combinations 1–12 with *Constant*, *Volumetric* and *Gangi* gave larger values than *Bai*, which gave the exact measured value with combinations 15 and 16. Among fracture models, in combinations 1–8, *Exponential* gave the smallest inflow, which was the one closest to the measured value, while *Constant* and *Angular* gave the largest inflows. Combined with *Bai* rock model, *Constant* and *Bed of Nails* fracture permeability models gave the smallest values. With *Gangi* rock model, changes between fracture models were too small to be observed.

Table 6: Inflow to hole 17G01 (ml/min, d = 76 mm), phase one, depth range 0.5–2.97 m.

Index	Model		Inflow
1	*Constant*	*Constant*	0.30
2	*Constant*	*Bed of Nails*	0.29
3	*Constant*	*Exponential*	0.28
4	*Constant*	*Angular*	0.30
5	*Volumetric*	*Constant*	0.30
6	*Volumetric*	*Bed of Nails*	0.29
7	*Volumetric*	*Exponential*	0.28
8	*Volumetric*	*Angular*	0.30
9	*Gangi*	*Constant*	0.29
10	*Gangi*	*Bed of Nails*	0.29
11	*Gangi*	*Exponential*	0.29
12	*Gangi*	*Angular*	0.29
13	*Bai*	*Constant*	0.21
14	*Bai*	*Bed of Nails*	0.21
15	*Bai*	*Exponential*	0.25
16	*Bai*	*Angular*	0.25
17	Measurement		0.25

Table 7: Inflow to hole 17G01 (ml/min, d = 300 mm), phase two, depth ranges I: 2.1–3.5 m, II: 2.95–3.5 m and III: 3.45–3.5 m.

Index	Model		I	II	III
1	*Constant*	*Constant*	0.47	0.27	0.07
2	*Constant*	*Bed of Nails*	0.48	0.28	0.09
3	*Constant*	*Exponential*	0.50	0.29	0.09
4	*Constant*	*Angular*	0.48	0.28	0.09
5	*Volumetric*	*Constant*	0.59	0.32	0.07
6	*Volumetric*	*Bed of Nails*	0.53	0.28	0.07
7	*Volumetric*	*Exponential*	0.55	0.29	0.07
8	*Volumetric*	*Angular*	0.54	0.29	0.07
9	*Gangi*	*Constant*	0.52	0.29	0.09
10	*Gangi*	*Bed of Nails*	0.50	0.29	0.09
11	*Gangi*	*Exponential*	0.58	0.34	0.12
12	*Gangi*	*Angular*	0.51	0.29	0.09
13	*Bai*	*Constant*	0.03	0.01	0.00
14	*Bai*	*Bed of Nails*	0.03	0.01	0.00
15	*Bai*	*Exponential*	0.04	0.02	0.01
16	*Bai*	*Angular*	0.04	0.01	0.01
17	Measurement		0.25	0.20	0.08

7.4.2 Inflow in phase two

The inflow measurements in phase two for 17G01 were conducted with two different methods: a nappy test and basic water collection. In a nappy test an absorbing mat, commonly called as a nappy, is placed on the studied area, and later the weight of the collected water is measured. The inflow test was conducted on three depth intervals: 2.1–3.5 m, 2.95–3.5 m and 3.45–3.5 m respectively. The simulation results are presented in Table 7. A graphical representation of the inflows computed for the three intervals with different model combinations can be found in Figure 14.

The measured relative inflow increased towards the bottom of the borehole. There were large differences between the models, but the simulation results can be divided into two groups: *Bai* combinations that gave smaller results, and the other models. Combinations 1–12 gave approximately twice as high values for interval I as what was measured, but close to measured values for interval III. Combinations 13–16 gave small values for all areas, though the relative inflow is greater in region III than what was measured. The inflow distribution along depth differed from the measured results with all combinations, as seen in Figure 14.

In the nappy inflow test simulation, the borehole was divided into 20-cm-high sections, as were the nappies, distributed over the depth interval 2.25–3.25 m. Nappy indexing goes from top to down. The numeric values for simulated inflow distributions are shown in Table 8. The inflow per nappy for each model combination and

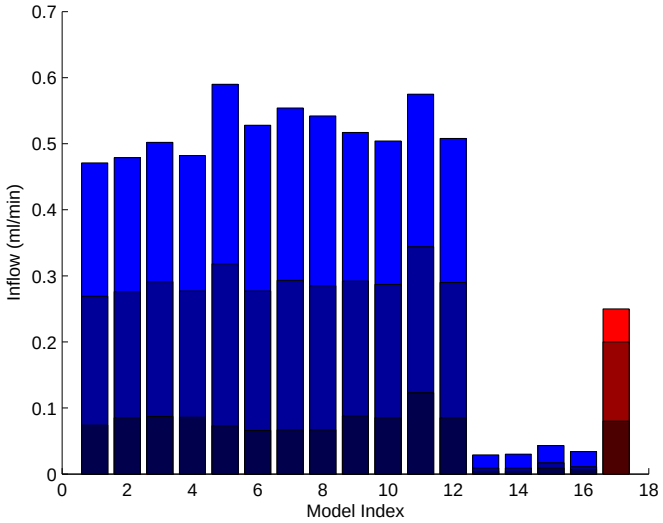

Figure 14: Inflow to three different sections of borehole 17G01, represented as the height of each column. The darkest color is for region III (3.45–3.5 m), middle color for II, (2.95–3.5 m), and brightest color is for region I (2.1–3.5 m). The red column presents the measured results.

the measurements are illustrated in Figure 15.

Model combinations 1–12 presented similar behaviour and large inflow values. Their inflow increased slightly with depth, with the exception of nappy 4, where a slight decrease of inflow was observed. Of rock models, *Volumetric* gave largest inflows, and *Constant* smallest values. The differences between the fracture models were relatively small. *Constant* and *Exponential* fracture models presented the largest differences.

Bai rock permeability model combinations 13–16 differed significantly from the others. Most importantly the results were small in value. Considering the inflow distribution, the greatest difference was that nappy 5 did not give the largest inflow, as in other models, but the smallest inflow. The shape of inflow along the depth was now first increasing and then decreasing. All four combinations had largest flow into nappies 2 and 3. Differences between the fracture models were negligible.

7.5 Inflow to borehole 18G01

The inflow to borehole 18G01 was measured only in phase two, for the depth interval of 2.1–3.1 m. Computed inflows for different model combinations and the measured values are presented in Table 9.

As with other results, combinations 1–12 exhibited similar behaviour, shown in Figure 16. They all gave large inflows with little variance between the fracture models. The inflows were close to what was simulated for 17G01 and even larger than what was measured for 17G01. *Bai* combinations 13–16 gave again small

Table 8: Inflow to hole 17G01 (ml/min, d = 300 mm), nappy test, depth range 2.25–3.25 m, nappy indexing runs downwards.

Model | Nappy	1	2	3	4	5
1	0.05	0.05	0.06	0.05	0.07
2	0.05	0.05	0.06	0.05	0.07
3	0.05	0.06	0.06	0.05	0.08
4	0.05	0.05	0.06	0.05	0.07
5	0.06	0.07	0.08	0.08	0.09
6	0.06	0.06	0.07	0.07	0.08
7	0.06	0.07	0.07	0.07	0.09
8	0.06	0.07	0.07	0.07	0.08
9	0.05	0.06	0.06	0.06	0.08
10	0.05	0.06	0.06	0.05	0.08
11	0.05	0.06	0.06	0.06	0.09
12	0.05	0.06	0.06	0.05	0.08
13	0.01	0.01	0.01	0.00	0.00
14	0.01	0.01	0.01	0.00	0.00
15	0.01	0.01	0.01	0.00	0.00
16	0.01	0.01	0.01	0.00	0.00
Measurement	0	0.023	0.016	0.015	0.024

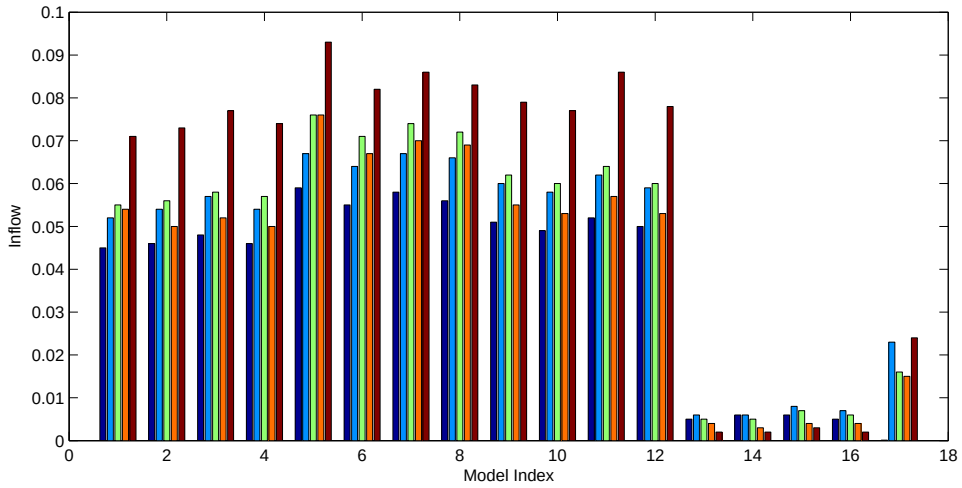

Figure 15: Nappytest simulations, inflows to 5 nappies computed with 16 different model combinations, index 17 presents the measurement results. Blue = nappy 1, light blue = nappy 2, green = nappy 3, orange = nappy 4, and red = nappy 5.

Table 9: Inflow to hole 18G01 (ml/min, d = 300 mm), phase two, depth range 2.1–3.1 m.

Index	Models		2.1–3.1
1	*Constant*	*Constant*	0.40
2	*Constant*	*Bed of Nails*	0.40
3	*Constant*	*Exponential*	0.42
4	*Constant*	*Angular*	0.41
5	*Volumetric*	*Constant*	0.52
6	*Volumetric*	*Bed of Nails*	0.44
7	*Volumetric*	*Exponential*	0.45
8	*Volumetric*	*Angular*	0.44
9	*Gangi*	*Constant*	0.43
10	*Gangi*	*Bed of Nails*	0.42
11	*Gangi*	*Exponential*	0.49
12	*Gangi*	*Angular*	0.43
13	*Bai*	*Constant*	0.01
14	*Bai*	*Bed of Nails*	0.01
15	*Bai*	*Exponential*	0.02
16	*Bai*	*Angular*	0.02
17	Measurement		0.03

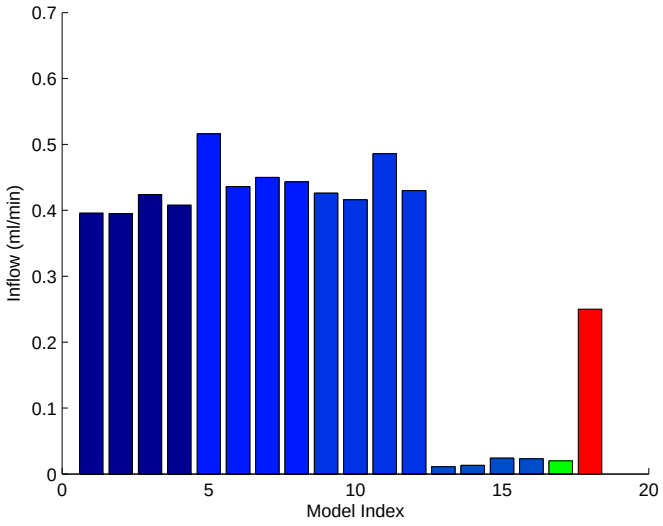

Figure 16: Inflow to borehole 18G01 at depth range 2.1–3.1 m, computed with different models (see indexes in Table 9). Measured inflow to 18G01 in green in index 17, and measured inflow to 17G01 in red in index 18 for comparison.

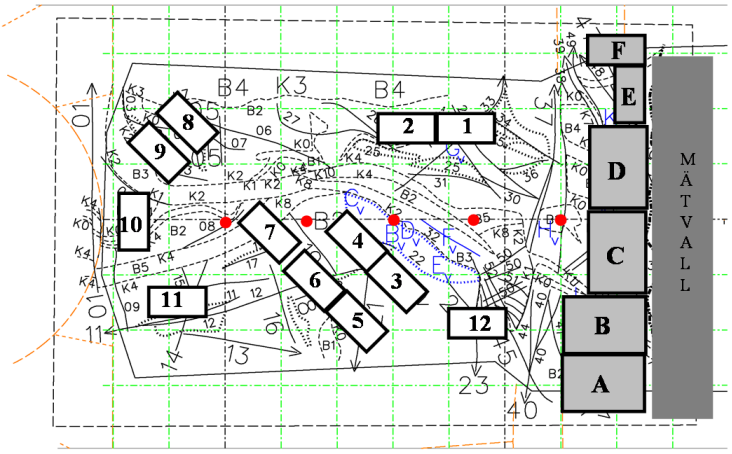

Figure 17: The approximate locations of the sorbing mats on TASO tunnel floor. MÄTVALL = measurement weir. Locations of the five boreholes are pointed in red [38].

inflows that were of the same order with the measured value. Orientation-dependent fracture models 15 and 16 gave larger results than the others.

7.6 Inflow to TASO tunnel

The inflow of water to TASO tunnel floor was measured with nappies. The nappies did not cover the whole area of the tunnel, but only places where inflow was observed; the placing of the nappies is presented in Figure 17. Nappies A to F were placed on the fracture-zone 1 and nappies 1–12 around the floor. Of nappies 1–12, 3 and 6 gave an inflow of 8 ml/min, and 2 and 10 2 ml/min, the rest gave smaller inflows. The inflows from the fracture zone are presented in Figure 18.

The simulation results of the tunnel floor showed increased flow close to the edges and at the end of the tunnel with all model combinations. The simulated floor–inflow profiles had two distinctive patterns based on rock model type. *Constant* and *Gangi* models gave maximum inflow at the end of the tunnel in the south corner, (Figure 19). The inflow decreased along the tunnel, faster with *Constant*, and was small close to the boreholes. Both models had increased inflow in the south corner of the wider part of the tunnel. In addition, *Gangi* presented increased inflow also at the ends of the intersection of the fracture-zone 1.

Bai and *Volumetric* rock models had increased flow along the edges of the tunnel, not directly on the edge of the floor, but approximately 30 cm from the walls as presented in Figure 19. *Bai* had its maximum inflow at the ends of fracture-zone-1 intersection. The maximum inflow of *Volumetric* was at the edges of the borehole 18 in the direction of the first principal strain. There was increased inflow also at the end of the tunnel. Both lattice models also presented increased flow at the same positions around the edges of hole 18. Fracture models affected the tunnel inflow only in the vicinity of fractures, close to the boreholes and two fracture zones. Mostly, the effects were slight, and differences in the general trends were not observed.

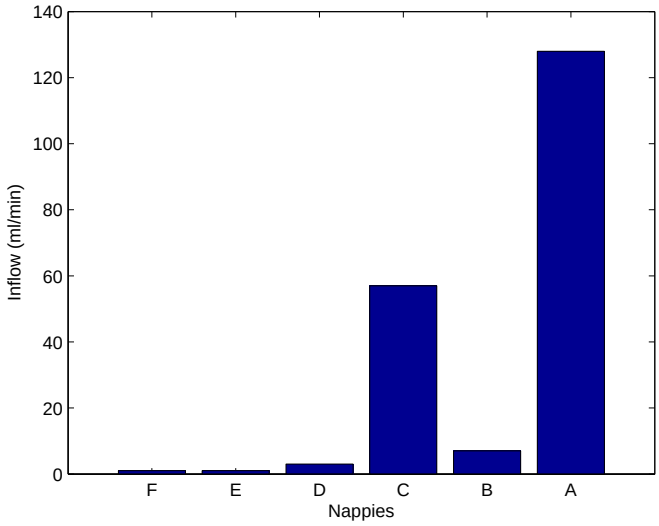

Figure 18: Inflow values measured from mats F–A.

The inflow from the fracture zone was controlled in the simulations by the fracture permeability model, although the rock permeability model played a role too. All model combinations presented a low peak at the location of mat F, as seen in Figure 20, unlike in the measurements in Figure 18. The outline of the inflow profile from the fracture-zone 1 intersection on TASO floor was quite similar with fracture models *Constant*, *Bed of Nails* and *Angular*. They all presented a peak inflow under mat A and a secondary peak under mat F. The relative size of the peaks depended on the rock permeability model. *Angular* gave small inflow, and *Exponential* was the only fracture model that presented a different profile. A sharp peak occurred approximately at mat B, and the zone of relatively large flow extended to mat C. A smaller peak was also observed on the other side, approximately between mats E and F, followed by a significant gap.

7.7 Pressure

The geometry and the permeability distribution determine the pressure contour in the study domain. Pressure measurements in Äspö were conducted in both phases, one borehole was sealed, sensors within, at the time, while all others were also sealed.

7.7.1 Phase one

The phase one pressure was measured from hole 17G01 from two depth intervals, 0.5–2.97 m and 2.0–2.97 m. The value measured for the first interval was 0.9–1 MPa, and for the latter 1.7 MPa. The modelled pressure distributions were close to each other, yielding for the first interval 0.2–0.9 MPa and at the second interval 0.6–1 MPa.

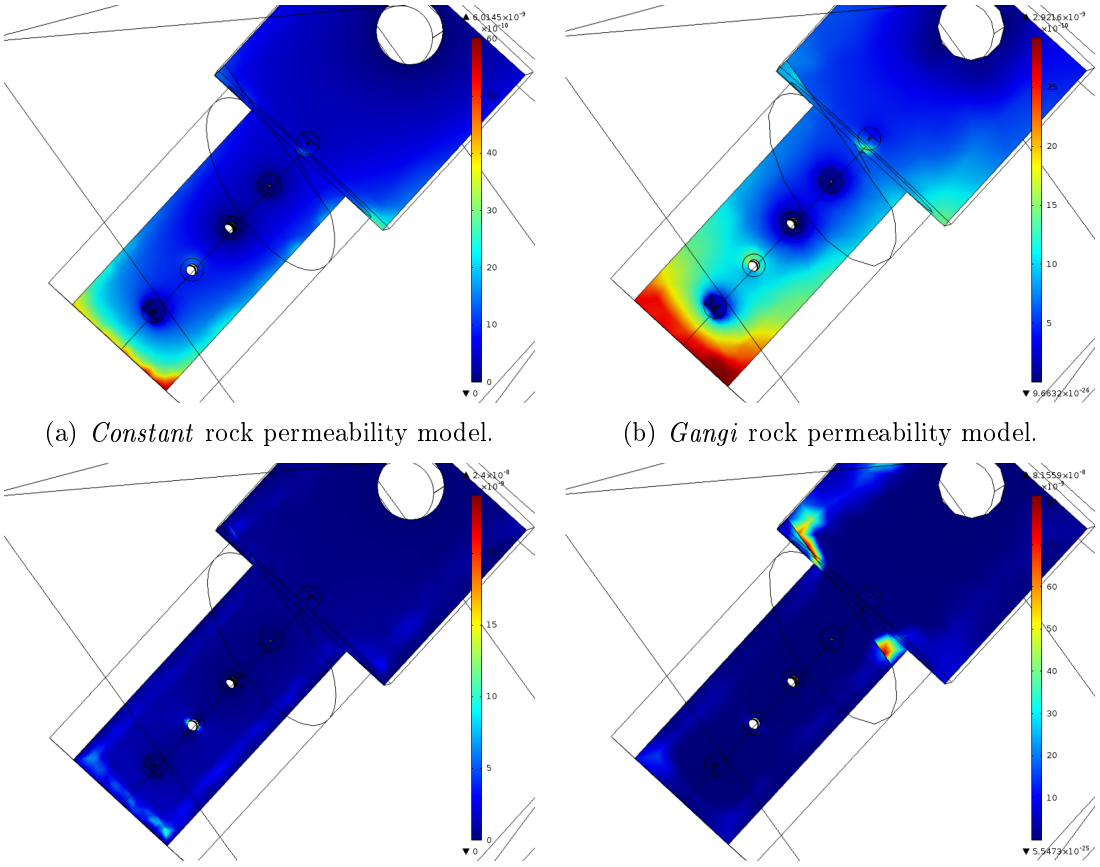

(a) *Constant* rock permeability model.

(b) *Gangi* rock permeability model.

(c) *Volumetric* rock permeability model.

(d) *Bai* rock permeability model.

Figure 19: Inflow distribution to TASO tunnel floor.

7.7.2 Phase two

In phase two there were measurement results from boreholes 15G01, 17G01, 18G01, the new boreholes 20G03, 20G04, and the new horizontal holes in the TASO walls 11A01, 11B01, 18A01 and 18B01. In phase two, *Bai* exhibited a different pressure behaviour close to the larger boreholes, and results from it are listed separately. The length intervals and both measured and computed pressures are listed in Table 10. The simulated pressure field around the boreholes while 17G01 is open is presented in Figure 21, and the pressure field around the horizontal boreholes is presented in Figure 22.

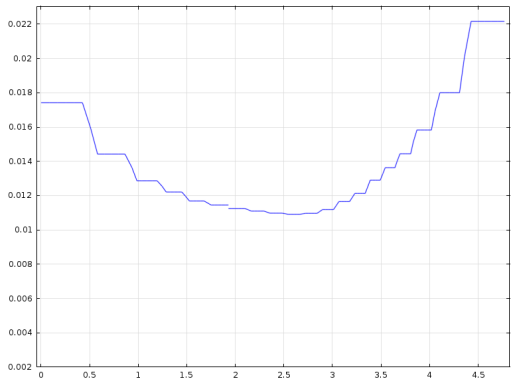

(a) *Constant* fracture permeability model.

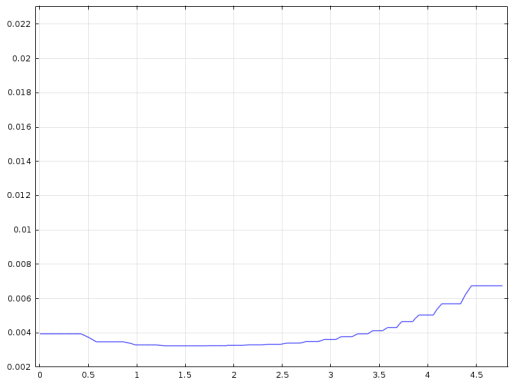

(b) *Angular* fracture permeability model.

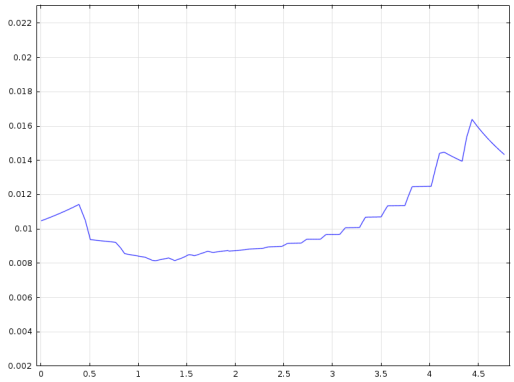

(c) *Bed of Nails* fracture permeability model.

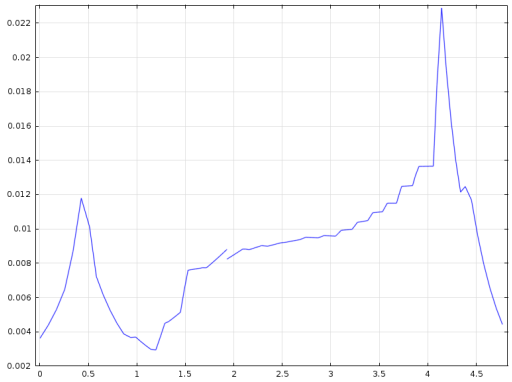

(d) *Exponential* fracture permeability model.

Figure 20: Outflow distribution profile from fracture zone 1 to TASO tunnel, computed with different fracture models and *Gangi* rock model. The layout is similar to Figure 18. Discontinuity in (d) is due to an intersecting line in the geometry. The relatively large element size is clearly visible in the figure.

Table 10: Measured and computed pressures for different boreholes in phase 2.

Borehole	Section (m)	P (MPa) Measured	P (MPa) 1–12	P (MPa) 13–16
15G01	2.1–3.03	0.5	0.6–0.7	0.4–0.6
17G01	2.11–2.97	0.5	0.7–0.9	0.12
18G01	1.42–3.06	0.4	0.7–1.1	0.1–0.12
20G04	2.0–3.5	1.05	1–1.4	0.9–1.3
20G03	2.0–3.5	0.9	0.9–1.3	0.6–1.2
11A01	1.01–10	2.7	0.5–1.9	0.5–1.9
11B01	1.24–10	0.3	0.3–1.1	0.3–1.1
18A01	1.11–10	2.6	0.6–2.6	0.6–2.6
18B01	1.28–10	2.1	0.4–1.5	0.4–1.5

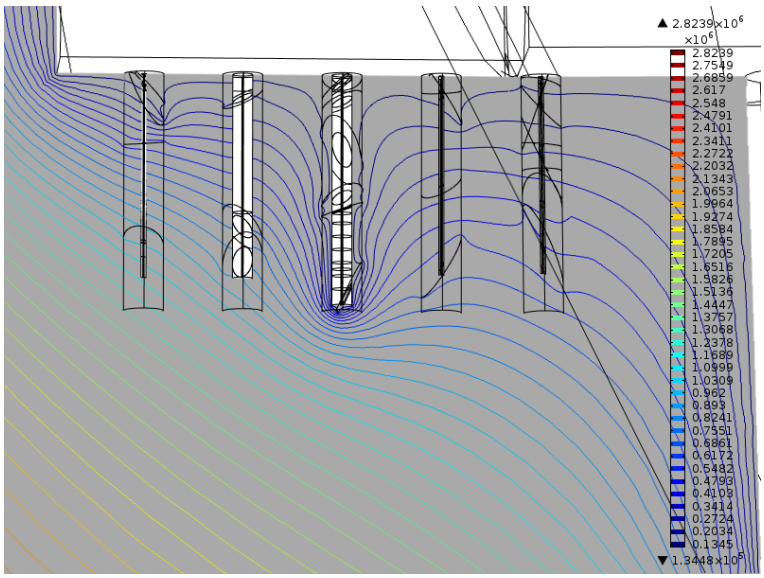

Figure 21: Pressure field around the boreholes, while borehole 17G01 is open.

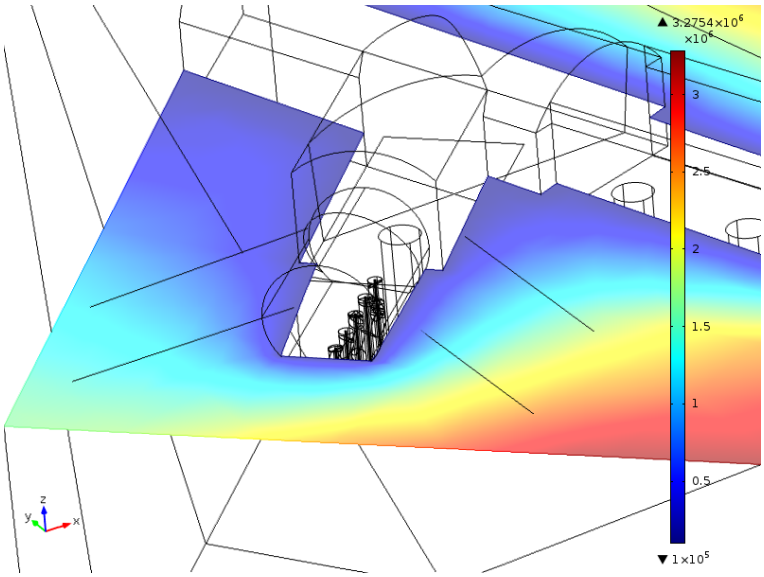

Figure 22: Pressure field around the horizontal boreholes (Pa).

8 Discussion

Sixteen combinations of rock and fracture permeability models were used for simulations of groundwater flow in stressed bedrock. Three rock permeability models and three fracture permeability models were used in addition to constant permeability models. The model naming and principles are presented in Table 1 and the model combination indexing is presented in Table 2. The simulations were conducted in two phases that have a different geometry; in phase one there were five boreholes of the same diameter, and in phase two, two of the boreholes were enlarged. All models were found to work well for the purpose of the simulation in phase one. In phase two, one of the rock permeability models poses numerical problems, but the other models give credible results. No single model can replicate the observed behaviour, but each model brings out different aspects of the phenomenon. From the results and calibration it is evident that the rock flow model dominates in a geometry such as in this work, mostly rock and a couple of fractures here and there.

8.1 Model implementation

The implementation of the model geometry leaves a lot of room for questions and errors, but when modelling in situ experiments, data is always lacking. Despite the systematic filtering procedure, including a few of the reported fractures is quite arbitrary and a lot of information from BIPS and core analysis is lost on the way. However, including observed fractures has more basis in reality than a completely statistical fracture network. During the elimination process of fractures before building the geometry, when two fractures are too close to each other, one is eliminated. The algorithm chooses the one placed first in the list to be eliminated, and no attention is paid on the fracture properties. Making this selection by hand would be slow, and a significant improvement in the result would not be guaranteed.

The models of phase two include all the same fractures as in the first phase and in addition the reported two new fractures. On the other hand, it is reported that only the two new fractures are identified as flowing structures in the enlarged boreholes. This could be interpreted so that only those two fractures should be included in the geometry. This choice would change the results especially in hole 18G01, and the upper parts of 17G01, and increase the importance of the rock permeability model even more. However, the translation from first phase geometry to the second phase would be even less consistent than at the moment.

The fracture size and shape is another thing that creates large uncertainties. All fractures are assumed planar, because there is no actual information on their shape. Also the radius chosen for the fractures is somewhat arbitrary. As there is no reported connectivity between the boreholes, it can only be assumed that the fractures do not cross fractures from different boreholes. Another source of conflict is that the permeability of the rock remains the same, even close to the boreholes, where the fractures are taken into account separately. The overall permeability around the boreholes is thus slightly increased. The importance of the rock permeability around the boreholes is increased, which could explain some of the differences

from the measurements. The calibration results would definitely be different, and the fracture flow would have a greater effect, which is more in line with the measurements. The phase two inflow measurements to 17G01 would have a different distribution, but the inflow result of hole 18G01 would not necessarily improve.

8.2 Inflow to borehole 17G01

The inflow tests to borehole 17G01 in phase one show only little difference between model combinations, which is not surprising as the models are calibrated based on the total inflow to this hole. Keeping this in mind, the inflow values from the length interval along the borehole, presented in Table 6, describe most importantly the distribution of the inflow along the hole. The results show that other rock models than *Bai* rock model tend to slightly overestimate the flow in the middle part of the borehole. *Bai* model gives the exact result or a slight underestimate, since it has a pronounced maximum flow point at the bottom of the hole. For the other models, the inflow from the bottom is smaller, since they have a smoother permeability distribution, hence the larger inflow to the measurement interval.

In phase two, the inflow was measured from three different depth intervals of the borehole. As seen in Figure 14, the measured relative inflow increases towards the bottom of the borehole. For model combinations 1–12 the inflow values are large, lacking such a relative increase of inflow with depth, as in the measurements. While there is difference in distribution, the inflow value from interval III is similar to what was measured. Rock permeability remains large and saturated close to the tunnel surface, and no clear change in distribution can be observed.

The bottom part of the borehole is dominated by the effect of the fracture added in phase two, the intersection goes through the bottom of the hole. The reason for the systematic difference of inflow distribution from the measurements by all models could be in the relative magnitude of rock and fracture permeability. High rock permeability overestimates flow in parts where there are no fractures, thus with lower rock permeability the distribution could be closer to measurements. The relative magnitude is a result of parameter choices made during the calibration. Another likely reason could be the geometry. The inflow distribution would be different if the measured fractures from phase one were not included. If the fracture at the bottom would be the only flowing structure, the amount of flow would be greater. Also, if the fracture were deeper, and especially, deeper than other fractures, the inflow distribution would be closer to what was measured.

With *Bai* model combinations 13–16 the inflow values are so small in all intervals that they are in the limits of the calibration accuracy, and the distribution is even further from what was measured than with the other combinations. This is due to the small pressure gradient around the enlarged boreholes. The flow distribution decreases downwards since the fracture flow to the bottom of the hole is very strong, and rock flow from regions close to fractures is diminished.

The general amount of inflow to the borehole increases due to the new fracture added in phase two, and the larger area. Another reason for an increase of flow is that the enlarged borehole has larger stresses and strains, which increase the

permeabilities. There is no total inflow value to the borehole reported, and hence it is difficult to estimate if the measured total inflow is actually larger in phase two.

8.3 Nappy test

A nappy test was performed on a section of borehole 17G01 in phase two. No model combination can replicate the measured nappy test results, neither in value nor structure. This is due to the measured zero value for nappy 1, which cannot be reached with models that have a non-zero permeability for rock. Also, the measurements report a flowing structure at nappy 2, which can also be seen from the nappy 2 inflow value. As the fracture is not included in the geometry, its effect cannot be seen in the simulation results. In the modelled geometry, the only fracture in the measurement area is at nappy 5.

The nappy test simulation results present the same divided behaviour as seen before. Three of the rock models, combinations 1–12, give similar results, where the rock model dominates so greatly that the differences between the fracture models can hardly be seen. The inflow distribution increases downwards in nappies 1–3, most likely due to the pressure distribution, nappy 4 gives a smaller value and nappy 5 the maximum. The decrease in nappy 4 flow is due to the fracture in nappy 5 that absorbs water from the nappy 4 area. *Bai* on the other hand gives very small results, with a different distribution, as was noticed also in phase two inflow to 17G01. A very small pressure gradient decreases the rock flow, and stronger fracture flow dominates. The flow decreases downwards in the measurement area, and the greatest difference to other models is that nappies 4 and 5 give the smallest values, instead of the maximum. All combinations have the maximum inflow at the bottom of the borehole, but since with *Bai* rock model the fracture flow is considerably stronger, a larger area around the fracture gets drained.

As can be seen in Figure 15, the rock model controls the distribution of the inflow, and the fracture model slightly changes the amount of inflow and the relative sizes between inflows to different nappies. Because there is only one fracture in the nappy test area, the significance of the fracture models is small. The relative difference of inflow between nappies 2 and 5 covering the observed fractures from the others, is around the same order in the measurements and combinations 1–12.

The zero inflow from nappy 1 raises questions of the inflow sources. The value may be a result from measurement inaccuracies, but the reason is probably in the relative magnitudes of rock and fracture flow. When considering the sources of the modelled flow, the two observed fractures at nappies 2 and 5 could form the flow of their respective nappies, but the source of the modelled inflow of nappies 3 and 4 is from the rock. However, if nappy 1 value is zero, the observed rock flow must be considered to consist of flow from fractures too small for observation, which is in line with the principle of the fracture lattice models. The lack of these fractures would explain the measured zero value. If this is the case, there is no way to predict or even replicate the inflow with *Constant* or *Volumetric* models. Although, adding a well conducting fracture to nappy 2 might decrease somewhat the inflow from nappy 1.

The inflow from the rock is quite high in the simulations, decreasing it could bring the results a lot closer to measurements.

8.4 Inflow to borehole 18G01

The computation of inflow to hole 18G01 brings out a significant difference between model predictions and the measurement. The reported inflow is very small, also compared to the reported inflow to 17G01. In models 1–12, the permeability of rock dominates so that even with no fractures in the model, the measured value of inflow would be exceeded. In addition, the two fractures at the lower part of the borehole both conduct well according to the fracture models. The second to lowest fracture is optimally oriented for both *Exponential* and *Angular* models. *Bai* model gives numerically very small values, but as with other combinations, larger values than the inflow values to hole 17G01. The measured inflow to 18G01 is only a small fraction of the inflow to 17G01.

In the measurements it was reported that at first there was no inflow to hole 18G01, and flowing started a while after the boring. This gives a strong indication that some sort of deformation might have happened, with the result of increased transmissivity. The fracture orientation of the phase two fracture is prone to deformation, when examined based on *Angular*. *Exponential* gives the fracture a shear to normal stress ratio $k_c \approx 2$, which could indicate dilation, depending on the friction angle of the fracture. The models could be used to find fractures that are prone to dilation.

8.5 Inflow to TASO tunnel floor

The simulated inflow patterns to the TASO tunnel floor vary between rock models, while fracture models have only small effects. The sorbing mats do not cover the whole floor, but since they were chosen based on visual inspections of the most flowing areas of the floor, other areas can be considered to have a smaller inflow. The sorbing mats can have absorbed water from the ground, falling water from the ceiling and the walls, but it is assumed here that all water comes from the floor.

The most significant inflow points of the floor, the points chosen by visual inspection for a mat location, are the fracture intersections. Thus the measurement result depends on the fracturing of the TASO floor. However, no fracture information of the floor was available when building the geometry, and thus in the models inflow to TASO consists of flow from rock mass. The differences between principles may seem large, but as in the fracture lattice models rock flow is essentially fracture flow, these models should be able to replicate the measurements to some extent. The area around borehole 18G01 is found to be more conductive, and several mats are placed around it in the measurements, as is the case at the end of the tunnel. These are found to match somehow with *Constant*, *Volumetric*, and especially *Gangi*. *Bai*, however, has an inflow maximum around nappies E and F, where barely any inflow is registered. Therefore, it can be concluded that *Bai* is far from what was measured.

Mats A to F in Figure 17 are placed on the deformation-zone 1, which is a heavily flowing structure, as in models as well. The heaviest flow comes from mats A and C, as mats E and F barely register any flow at all. As the sorbing mat test does not separate the flow out of the fracture zone from the flow out of the rock, it can only be assumed that majority of the water comes from the fracture. With this assumption the inflow profiles along fracture zone intersection in Figure 20 can be compared with the measured inflow in Figure 18. All profiles are flat when compared to the measured profile, and all have a peak at nappy F. *Constant* fracture model profile, Figure 20(a) is least similar to the measurements. *Exponential* is the only fracture model taking the shear stress into account, and that can be seen from the more complex inflow profile.

All models have the small peak at mat F since the corner is an inflow point for a large area of the fracture. However, this phenomenon is completely lacking from the measurements. This could indicate that the north side of the tunnel has decreased flow compared to the south side. This theory is supported also by the horizontal pressure measurements. This is partly due to the other tunnel (Figure 3) that is close to TASO on the northern side.

8.6 Pressure measurements

The pressure fields are realistic, follow the measurements to a large extent, and the pressure values give insight to the fracture connectivity. Only *Bai* has in some cases a significantly different pressure distribution from the others. The high maximum permeability values of *Bai* near the expanded boreholes of the phase two geometry cause the pressure in these boreholes to drop to the tunnel boundary pressure, whatever their boundary condition.

In phase one the measured pressure for the first interval of 17G01 is of the same order than what is computed at the lower level of the interval. More extensive connectivity at the topmost part could account for the measured high pressure for the whole distance. At the lower part of the borehole, the measured pressure is large, 2.7 MPa compared to the simulated 0.6–1 MPa. This indicates a good connectivity to much deeper in the bedrock, for example a deep fracture.

In phase two the measured pressure values for the original G01 type boreholes are slightly smaller than those given by combinations 1–12. *Bai* values are in general slightly smaller than the others, and in some cases give a slightly better estimate due to the smaller values. However, for the enlarged boreholes 17G01 and 18G01 *Bai* combinations give very small pressures, due to the large total permeability around the enlarged boreholes. Between the two phases of the experiment, the measured pressure in hole 17G01 decreases significantly. The enlargement of the borehole seems to destroy some connection deeper to the rock.

In the case of the horizontal boreholes, as they are 10 meters long, they cover quite a range of pressures in the model. The measured pressure values are large, except the inner pressure on the B side. 11A01 is clearly well connected to the deeper parts, away from the tunnels, as the measured pressure value is so high, seen in Table 10. Both holes at the end of the tunnel give quite large measured values. 11B01

on the other hand is placed between tunnels, as seen in Figure 3, hence the smaller simulated values. The differences from the simulated pressure fields would lead to conclude that there are higher pressures around TASO than what the simulations suggest, with the exception of 11B01 that is well connected with the low pressure area between tunnels.

Overall the pressure measurements showed that the models are close to what is measured, but there are some over- and underestimates. Too large simulated pressures are found in the vicinity of the tunnel, and too small can be found particularly in the long horizontal boreholes. The underestimates could be corrected by changing the pressure boundary condition, but a more probable and less practical cause of error is the lacking fracture and connectivity data. The tendency could indicate that the permeability is in general larger close to the tunnel and smaller deep in the rock.

8.7 Comparison of the models

The model results showed a divided behaviour. *Constant*, *Volumetric* and *Gangi* rock models give similar results in shape and magnitude, while *Bai* combinations give markedly different results. Except for this division, differences between models were small. There is no single model that would outperform the others, but better models can be named, depending on the type of results wanted. It makes a difference if a better value for inflow, or a more accurate inflow distribution is wanted, when comparing the models.

Constant and *Gangi* are similar to some extent, even though one is isotropic and the other diagonal, since the change in permeability magnitude in *Gangi* is less than an order of magnitude per component. In *Bai*, on the other hand, the change is five orders of magnitude per component and the permeability is diagonal. This causes large permeability magnitudes, and significant differences between directions, which lead to numerical problems. *Volumetric* has permeability varying for more than ten orders of magnitude, with no problems during solving, due to its isotropy.

The differing results of *Bai* in phase two are due to its quickly changing permeability and a resulting differently shaped pressure distribution. Around the expanded boreholes the total permeability is large due to large strains, and this large permeability draws down the small pressures of the tunnel floor. This leads to a small pressure gradient along the surface of the borehole, and a large gradient right below the borehole. The pressure along the borehole evens out, leading to the impression that the hole is under an atmospheric pressure boundary condition even if it is not. This only happens with the enlarged boreholes. With *Volumetric* such very large changes of permeability magnitude around the hole take place, but there are both small and large total permeabilities around the borehole, and no such change in the pressure distribution occurs.

Constant rock model gives slightly larger results for 17G01 in phase one due to its relatively even inflow distribution, and in phase two it gives the smallest results of combinations 1–12, that are still large compared to measurements. Both *Volumetric* and *Gangi* models have significantly larger inflows around the borehole

due to permeability variation. The same case is in 18G01. The values are smallest since there are no large permeability areas around boreholes, such as the other models have. *Constant* rock model is a good choice if the best numeric values are wanted, but even those inflows are significantly larger than measurements, and other models describe the distribution of the flow better.

Volumetric rock model gives roughly the largest results in every measurement. With this model also the inflow distribution to 17G01 is the worst, since the volumetric strain is constant along vertical lines, preventing the observed vertical differences from forming, which can be seen in Figures 14 and 15. *Gangi* falls between *Constant* and *Volumetric* when it comes to inflow values and profiles. This follows its formulation, which can be considered as constant, but is slightly stress dependent. Its permeability around the boreholes is vertically constant, as with the Volumetric model. *Gangi* combination 11 gives the best distribution of flow into 17G01 in phase two.

Bai gives the least correct results in phase two with the small inflows and opposite distributions from measurements and other models. Also from the TASO inflow test, the only actual conclusion that can be made is that *Bai* results do not fit. The permeability causes a very small pressure gradient around the enlarged boreholes. In this model also the relative magnitude of fracture flow is much larger than mostly in other combinations. On the other hand, the measured pressures and inflows are smaller than what was simulated with other combinations, and in several cases *Bai* gives better results. This could indicate that the pressure distribution of *Bai* could have some resemblance to the measured distribution. Such increased permeability around the boreholes, as with *Bai*, that changes the pressure distribution, could give the measured smaller inflows and smaller pressures. Also, in phase one *Bai* gives the best results.

Of the fracture models, *Bed of Nails* gives the smallest inflows. This is due to the mathematical formulation of the model that only allows compression. *Angular* is close to *Bed of Nails* in values, the range of permeability is not radical in this model either. *Constant* fracture model inflow values are large, when combined to the other rock models than *Constant*, since *Constant* fracture model transmits water equally from all over. *Exponential* has dilation included and gives larger values due to this property. The magnitude of flow is partially due to the choice $k_c = 1$, made in the implementation. The value is what has been measured for single fractures, but simulated values for fracture systems are larger. The inflow distribution of *Exponential* from fracture zone 1, Figure 20(c), could be called slightly better than the others. It has a distinct peak and, if not for the peak at nappy F, would resemble the measured inflow in Figure 18. Also, combination 11 with *Exponential* in the phase two inflow to 17G01 has a slightly better distribution than the others.

Differences between modelled results tend to be small, when comparing the modelled and measured results, which indicates that the inequality to the measurement results is caused mainly by conceptual differences.

9 Conclusions

The effect of stress state on bedrock permeability for groundwater was studied by simulating an in situ experiment. The dependency of permeability on stress was computed with different relations, not by making the conventional assumption that hydraulic and mechanical apertures are equal. The approach was found to work well for in situ simulations.

Two permeability models were implemented as such, three of the models were developed further to suit the implementation, and a new empirical model for fracture permeability was derived from previously reported experimental results. The simulation geometry was constructed based on the experimental setup of BRIE. COMSOL was found to be a sufficient tool for the simulations in the applied geometry, wherein the number of fractures had been reduced.

Due to the geometry implementation and calibration, the effect of rock permeability was pronounced. The granular approach of the rock structure did not work well for the studied rock type, neither as compressive grains in a symmetric lattice (Eq. (36), Eq. (38)), nor as randomly placed incompressive grains (Eq. (35)). A constant rock permeability or a fracture lattice model were found to be more suitable for the studied rock. Two of the fracture models (*Exponential* and *Angular*) were found to be able to roughly estimate the tendency of fractures to displace and dilate.

In the future, different model geometry and calibration parameters should be tested in order to estimate their effect on results. Fracture lattice models should be applied in line with the fracture models, and different in situ sites could be tried out. Comparison with DFN computations would give insight into the consequences of the choice of concept. The mechanical model could be improved by including the fractures, if stiffness data were available. With the help of the aforementioned study suggestions, a suitable model for permeability for the studied rock type can be found, and the presented method could be used in in situ modelling tasks.

References

[1] L. Qiao, R. Wong, R. Aguilera, and A. Kantzas. Determination of Biot's effective stress parameter for permeability of Nikanassin sandstone. In *Canadian International Petroleum Conference*, 2009.

[2] C.J. Talbot and M. Sirat. Stress control of hydraulic conductivity in fracture-saturated Swedish bedrock. *Engineering geology*, 61(2):145–153, 2001.

[3] S.F. Rogers. Critical stress-related permeability in fractured rocks. *Geological Society, London, Special Publications*, 209(1):7–16, 2003.

[4] K. Min, L. Jing, and O. Stephansson. Determining the equivalent permeability tensor for fractured rock masses using a stochastic REV approach: method and application to the field data from Sellafield, UK. *Hydrogeology Journal*, 12(5):497–510, 2004.

[5] C.B. Zhou, R.S. Sharma, Y.F. Chen, and G. Rong. Flow–stress coupled permeability tensor for fractured rock masses. *International journal for numerical and analytical methods in geomechanics*, 32(11):1289–1309, 2008.

[6] A. Baghbanan and L. Jing. Stress effects on permeability in a fractured rock mass with correlated fracture length and aperture. *International Journal of Rock Mechanics and Mining Sciences*, 45(8):1320–1334, 2008.

[7] Z. Zhao, L. Jing, I. Neretnieks, and L. Moreno. Numerical modeling of stress effects on solute transport in fractured rocks. *Computers and Geotechnics*, 38(2):113–126, 2011.

[8] M.A. Biot. General theory of three-dimensional consolidation. *Journal of applied physics*, 12(2):155–164, 1941.

[9] W.D. Carrier III. Goodbye, Hazen; Hello, Kozeny-Carman. *Journal of Geotechnical and Geoenvironmental Engineering*, 129(11):1054–1056, 2003.

[10] J. Kozeny. Über kapillare Leitung des Wassers im Boden. *Sitzungsber. Akad. Wiss. Wien*, 136:271–306, 1927.

[11] P.C. Carman. Fluid flow through granular beds. *Transactions-Institution of Chemical Engineeres*, 15:150–166, 1937.

[12] I. Fatt and D.H. Davis. Reduction in permeability with overburden pressure. *Journal of Petroleum Technology*, 4(12), 1952.

[13] J.P. Davies and D.K. Davies. Stress-dependent permeability: characterization and modeling. *SPE Journal*, 6(2):224–235, 2001.

[14] A.F. Gangi. Variation of whole and fractured porous rock permeability with confining pressure. *International Journal of Rock Mechanics and Mining Sciences & Geomechanics Abstracts*, 15(5):249–257, 1978.

[15] M. Bai and D. Elsworth. Modeling of subsidence and stress-dependent hydraulic conductivity for intact and fractured porous media. *Rock mechanics and rock engineering*, 27(4):209–234, 1994.

[16] M. Bai, F. Meng, D. Elsworth, M. Zaman, and J.C. Roegiers. Numerical modeling of stress-dependent permeability. *International Journal of Rock Mechanics and Mining Sciences*, 34(3):2–e1, 1997.

[17] J.M. Kim and R.R. Parizek. A mathematical model for the hydraulic properties of deforming porous media. *Ground Water*, 37(4):546–554, 1999.

[18] J. Boussinesq. Memoire sur l'influence des frottements dans les mouvements reguliers des fluides. *J. Liouville*, 13:377–424, 1868.

[19] C. Louis. *A study of groundwater flow in jointed rock and its influence on the stability of rock masses.* Imperial College of Science and Technology, 1969.

[20] D.T. Snow. Rock fracture spacings, openings, and porosities. *Journal of Soil Mechanics & Foundations Div*, 1968.

[21] F. Jones Jr. A laboratory study of the effects of confining pressure on fracture flow and storage capacity in carbonate rocks. *Journal of Petroleum Technology*, 27(1):21–27, 1975.

[22] P.A. Witherspoon, J.S.Y. Wang, K. Iwai, and J.E. Gale. Validity of cubic law for fluid flow in a deformable rock fracture. *Water Resources Research*, 16(6):1016–1024, 1980.

[23] J.A. Greenwood and J.B.P. Williamson. Contact of nominally flat surfaces. *Proceedings of the Royal Society of London. Series A. Mathematical and Physical Sciences*, 295(1442):300–319, 1966.

[24] P.A. Witherspoon and J.E. Gale. Mechanical and hydraulic properties of rocks related to induced seismicity. *Engineering Geology*, 11(1):23–55, 1977.

[25] G. Swan. Determination of stiffness and other joint properties from roughness measurements. *Rock Mechanics and Rock Engineering*, 16(1):19–38, 1983.

[26] J.E. Gale. The effects of fracture type (induced versus natural) on the stress-fracture closure-fracture permeability relationships. In *The 23rd US Symposium on Rock Mechanics (USRMS)*, 1982.

[27] I.W. Yeo, M.H. De Freitas, and R.W. Zimmerman. Effect of shear displacement on the aperture and permeability of a rock fracture. *International Journal of Rock Mechanics and Mining Sciences*, 35(8):1051–1070, 1998.

[28] S. Gentier, E. Lamontagne, G. Archambault, and J. Riss. Anisotropy of flow in a fracture undergoing shear and its relationship to the direction of shearing and injection pressure. *International Journal of Rock Mechanics and Mining Sciences*, 34(3):94–e1, 1997.

[29] H.S. Lee and T.F. Cho. Hydraulic characteristics of rough fractures in linear flow under normal and shear load. *Rock Mechanics and Rock Engineering*, 35(4):299–318, 2002.

[30] Z. Chen, S.P. Narayan, Z. Yang, and S.S. Rahman. An experimental investigation of hydraulic behaviour of fractures and joints in granitic rock. *International Journal of Rock Mechanics and Mining Sciences*, 37(7):1061–1071, 2000.

[31] K.B. Min, J. Rutqvist, C.F. Tsang, and L. Jing. Stress-dependent permeability of fractured rock masses: a numerical study. *International Journal of Rock Mechanics and Mining Sciences*, 41(7):1191–1210, 2004.

[32] B.H.G. Brady and E.T. Brown. *Rock mechanics: for underground mining*. Springer, 2007.

[33] J. Zhang, W.B. Standifird, J-C. Roegiers, and Y. Zhang. Stress-dependent fluid flow and permeability in fractured media: from lab experiments to engineering applications. *Rock mechanics and rock engineering*, 40(1):3–21, 2007.

[34] Kang Feng and Zhongci Shi. *Mathematical theory of elastic structures*. Springer Berlin, 1996.

[35] E. Hakami. *Aperture distribution of rock fractures*. PhD thesis, Royal Institute of Technology Stockholm, Sweden, 1995.

[36] T. Koyama, N. Fardin, L. Jing, and O. Stephansson. Numerical simulation of shear-induced flow anisotropy and scale-dependent aperture and transmissivity evolution of rock fracture replicas. *International Journal of Rock Mechanics and Mining Sciences*, 43(1):89–106, 2006.

[37] COMSOL Multiphysics. `www.comsol.com`. 1.2.2013.

[38] Å. Fransson and M. Åkesson. Äspö Hard Rock Laboratory, Bentonite Rock Interaction Experiment. SKB X-XX-XX, To be published.

Series title and number
VTT Technology 127

Title	**The effect of stress state on groundwater flow in bedrock** **Simulations of in situ experiments**
Author(s)	Karita Kajanto
Abstract	The effect of the stress state on the permeability of bedrock for groundwater was studied by simulating an in situ experiment. Previous studies show that the dependency of permeability on stress can have a significant effect on flow. Several models have been developed, but little has been done in order to develop models suitable for in situ applications, such as the deep underground repositories for spent nuclear fuel. In repositories, stress state evolves during the long time period considered in safety assessment. The effect of the changing flow pattern, due to the evolving stress, has to be estimated for, e.g., radionuclide transport calculations. Previous work done in the field was reviewed, existing relations between stress and permeability were analysed, and suitable relations were selected for the modelling cases. Rock mass permeability and discrete fracture permeability were treated separately. One new empirical model for fracture permeability was presented and three models were further developed to be more suitable for 3-D implementation. Simulations followed in situ experiments conducted in Äspö Hard Rock Laboratory. The modelling geometry was constructed based on the experimental setup and the fracture information from the location. The overall stress state in the area was known and the effect of the measurement tunnel and boreholes was computed. The stress state was used to compute the groundwater flow, and the applicability of the chosen models for in situ modelling was analysed. COMSOL Multiphysics was used as the tool for the simulations. The simulation results followed the measurements reasonably well, but differences were found with one model. The results show that differences between most of the models were relatively small if inflow rates were compared, however, differences between flow patterns were found. Stress dependency could partly explain observed phenomena and qualitative behaviour. Moreover, some of the fracture models were able to identify fractures prone to deformation.
ISBN, ISSN	ISBN 978-951-38-8054-5 (URL: http://www.vtt.fi/publications/index.jsp) ISSN-L 2242-1211 ISSN 2242-122X (Online)
Date	September 2013
Language	English, Finnish abstract
Pages	59 p.
Name of the project	
Commissioned by	
Keywords	Permeability, stress, in situ, bedrock, groundwater
Publisher	VTT Technical Research Centre of Finland P.O. Box 1000, FI-02044 VTT, Finland, Tel. 020 722 111

Julkaisun sarja ja numero
VTT Technology 127

Nimeke	**Jännitystilan vaikutus pohjaveden virtaukseen kallioperässä** **Paikkatutkimustulosten mallinnusta**
Tekijä(t)	Karita Kajanto
Tiivistelmä	Jännitystilan vaikutusta kallioperän permeabiliteettiin vedelle tutkittiin simuloimalla in situ -tilannetta. Aiemmat tutkimukset ovat osoittaneet, että permeabiliteetin riippuvuus jännitystilasta voi vaikuttaa merkittävästi kallion pohjavesivirtaukseen. Erilaisia malleja aiheesta on kehitetty, mutta in situ -mallinnukseen soveltuvien mallien kehitys on jäänyt vähemmälle. Turvallisuusanalyysin pitkän ajanjakson aikana jännitystila kalliossa loppusijoitussyvyydellä muuttuu. Muuttuvan jännityksen virtaukseen aiheuttamat muutokset tulee ottaa huomioon radionuklidien kulkeutumislaskennassa. Tässä työssä käytiin läpi alan aiempia tutkimuksia, analysoitiin kehitettyjä jännityksen ja permeabiliteetin välisiä malleja sekä valittiin erilaisia tutkittavalle kivityypille soveltuvia malleja mallinnustapauksissa käytettäviksi. Kiviaineksen permeabiliteettia ja yksittäisten rakojen permeabiliteettia käsiteltiin erikseen. Uusi empiirinen rakopermeabiliteettimalli esiteltiin ja aiempia malleja kehitettiin paremmin in situ -mallinnukseen sopiviksi. Simulaatiotapaukset laadittiin Äspö Hard Rock Laboratoryssa tehtyjen mittausten mukaisesti. Laskentageometria vastasi koejärjestelyjä ja alueelta tehtyjä havaintoja. Alueen keskimääräinen jännitystila tunnetaan, ja sen avulla laskettiin mittaustunnelin ja reikien vaikutus mallinnusalueella. Valittujen mallien soveltuvuutta in situ -mallinnukseen analysoitiin. Laskenta suoritettiin COMSOL Multiphysics -ohjelmistolla. Mallien tulokset noudattivat mittauksia in situ -mallinnustuloksiksi hyvin, mutta joissain tapauksissa esiintyi selviä eroja. Virtaamatuloksien väliset erot useiden mallien kesken olivat suhteellisen pieniä. Virtausjakaumista löytyi selkeitä eroja, ja jännitystilariippuvuudella voinee selittää joitain tuloksia ja käyttäytymistä. Lisäksi havaittiin, että eräillä rakomalleilla pystyy tunnistamaan raot, joilla on muita suurempi todennäköisyys deformaatioon.
ISBN, ISSN	ISBN 978-951-38-8054-5 (URL: http://www.vtt.fi/publications/index.jsp) ISSN-L 2242-1211 ISSN 2242-122X (verkkojulkaisu)
Julkaisuaika	Syyskuu 2013
Kieli	Englanti, suomenkielinen tiivistelmä
Sivumäärä	59 s.
Projektin nimi	
Toimeksiantajat	
Avainsanat	Permeability, stress, in situ, bedrock, groundwater
Julkaisija	VTT PL 1000, 02044 VTT, Puh. 020 722 111

The effect of stress state on groundwater flow in bedrock

Simulations of in situ experiments

ISBN 978-951-38-8054-5 (URL: http://www.vtt.fi/publications/index.jsp)
ISSN-L 2242-1211
ISSN 2242-122X (Online)

VTT TECHNOLOGY 127 The effect of stress state on groundwater flow in bedrock